Evaluation of extreme precipitation based on three long-term gridded products over the qinghai-tibet plateau

He, Qingshan; Yang, Jianping; Chen, Hongju; Liu, Jun; Ji, Qin; Wang, Yanxia; Tang, Fan

Published in:
Remote Sensing

Link to article, DOI:
10.3390/rs13153010

Publication date:
2021

Document Version
Publisher's PDF, also known as Version of record

remote sensing

MDPI

Article

Evaluation of Extreme Precipitation Based on Three Long-Term Gridded Products over the Qinghai-Tibet Plateau

Qingshan He [1,2], Jianping Yang [1,*], Hongju Chen [1,2], Jun Liu [3], Qin Ji [1,2], Yanxia Wang [1,2] and Fan Tang [1,2]

[1] State Key Laboratory of Cryospheric Sciences, Northwest Institute of Eco-Environment and Resources, Chinese Academy of Sciences, Lanzhou 730000, China; heqingshan@nieer.ac.cn (Q.H.); chenhongju@nieer.ac.cn (H.C.); jiqin@lzb.ac.cn (Q.J.); wangyanxia@nieer.ac.cn (Y.W.); tangfan@nieer.ac.cn (F.T.)
[2] University of Chinese Academy of Sciences, Beijing 100049, China
[3] Department of Environmental Engineering, Technical University of Denmark, 2800 Kongens Lyngby, Denmark; juli@env.dtu.dk
* Correspondence: jianping@lzb.ac.cn

Abstract: Accurate estimates of extreme precipitation events play an important role in climate change studies and natural disaster risk assessments. This study aimed to evaluate the capability of the China Meteorological Forcing Dataset (CMFD), Asian Precipitation-Highly Resolved Observational Data Integration Towards Evaluation of Water Resources (APHRODITE), and Climate Hazards Group Infrared Precipitation with Station data (CHIRPS) to detect the spatiotemporal patterns of extreme precipitation events over the Qinghai-Tibet Plateau (QTP) in China, from 1981 to 2014. Compared to the gauge-based precipitation dataset obtained from 101 stations across the region, 12 indices of extreme precipitation were employed and classified into three categories: fixed threshold, station-related threshold, and non-threshold indices. Correlation coefficient (CC), root mean square error (RMSE), mean absolute error (MAE), and Kling–Gupta efficiency (KGE), were used to assess the accuracy of extreme precipitation estimation; indices including probability of detection (POD), false alarm ratio (FAR), and critical success index (CSI) were adopted to evaluate the ability of gridded products' to detect rain occurrences. The results indicated that all three gridded datasets showed acceptable representation of the extreme precipitation events over the QTP. CMFD and APHRODITE tended to slightly underestimate extreme precipitation indices (except for consecutive wet days), whereas CHIRPS overestimated most indices. Overall, CMFD outperformed the other datasets for capturing the spatiotemporal pattern of most extreme precipitation indices over the QTP. Although CHIRPS had lower levels of accuracy, the generated data had a higher spatial resolution, and with correction, it may be considered for small-scale studies in future research.

Keywords: CMFD; APHRODITE; CHIRPS; extreme precipitation; Qinghai-Tibet Plateau

Citation: He, Q.; Yang, J.; Chen, H.; Liu, J.; Ji, Q.; Wang, Y.; Tang, F. Evaluation of Extreme Precipitation Based on Three Long-Term Gridded Products over the Qinghai-Tibet Plateau. *Remote Sens.* **2021**, *13*, 3010. https://doi.org/10.3390/rs13153010

Academic Editor: Elisa Palazzi

Received: 1 July 2021
Accepted: 28 July 2021
Published: 30 July 2021

1. Introduction

Extreme precipitation events are associated with natural flooding disasters that have devastating impacts on the infrastructure, local economies, and human lives [1,2]. As a region sensitive to climate change, the Qinghai-Tibet Plateau (QTP) is particularly prone to natural hazards, such as debris flow from landslides, flash floods, and glacial lake outburst floods [3,4]. Precipitation plays a central role in the cryosphere and climate; however, there is limited relevant research on this because of the scarcity of conventional meteorological data. Thus, high quality and gridded precipitation datasets are vital for the concerted effort on drought monitoring, extreme climate analyses, and natural hazard risk assessments [5–7].

In recent decades, extensive studies have been conducted to evaluate the performance of precipitation products at the local and regional scales. For example, the assessment of gridded precipitation products such as Multi-Source Weighted-Ensemble Precipitation

(MSWEP) and Climate Hazards Group InfraRed Precipitation with Station data (CHIRPS) in mainland China [5,8], and across the entirety of the QTP [9]; China Meteorological Forcing Dataset (CMFD), Tropical Rainfall Measuring Mission (TRMM), and CHIRPS in the QTP [10]; Asian Precipitation-Highly Resolved Observational Data Integration Towards Evaluation of Water Resources (APHRODITE), Precipitation Estimation from Remotely Sensed Information using Artificial Neural Networks–Climate Data Record (PERSIANN-CDR), and CHIRPS in the QTP [11]; TRMM and Integrated Multi-satellite Retrievals for GPM (IMERG) over the QTP [12] and Hexi Corridor [13]; Climate Prediction Center's morphing technique (CMORPH) over the QTP [14]. The overall results showed that there are distinct differences and biases between rain-gauge networks. Furthermore, the regions characterized by complex topography, precipitation estimates can be associated with significant error, because of high spatiotemporal variability and uncertainty controlled by the orography [15–17].

The accuracy evaluation of extreme precipitation events derived from gridded precipitation products are crucial for flood and drought monitoring, especially in the relatively sparse rain-gauge network areas [18]. These products are particularly important in complex topography, where rain gauges are generally distributed in lowlands, thus the precipitation occurring in highlands is underrepresented. For these regions, satellite-based precipitation (SBP) products may be the only source to fill this important data gap. [16]. Currently, several studies on assessing extreme precipitation events using gridded products on a regional scale are available in the literature, such as the reports on the United States [19], Brazilian Amazonia [20], Sub-Saharan Africa [21], Southeast Asia [22], China [23,24], the Loess Plateau [25], and the three-rivers headwater region of China [26]. In summary, the accuracy of extreme precipitation products varies with regions, and spatiotemporal scales. However, extreme precipitation evaluations are lacking in the QTP. Thus, three long-term gridded precipitation datasets were considered in this study—CMFD, APHRODITE, and CHIRPS 2.0. The main reasons we chose these three precipitation datasets were that (1) all have high spatial resolution (0.05 ~ 0.25°); (2) all provide daily precipitation records up to 30 years which could greatly improve the accuracy of extreme precipitation prediction; (3) according to previous studies [9–11], these three datasets have different performance advantages with regard to the study on QTP.

In this study, we compared 12 indices of extreme precipitation to the results of annual precipitation scales based on the three gridded products and 101 rain-gauge stations over the QTP. This study aimed to evaluate the accuracy and applicability of the gridded products for characterizing extreme precipitation events over the entire QTP and to determine whether these products are suitable for long-term monitoring of extreme precipitation events in the QTP. This paper is structured as follows: a brief introduction of the QTP; methods and data are presented in Section 2; Section 3 contains the results and discussion of the findings, including the evaluation results of the rainfall extremes from the different datasets at the monthly and annual scales; conclusions are presented in Section 4.

2. Data and Methods

2.1. Study Area

As the highest geomorphic unit on the earth, the QTP is known as the 'roof of the world' (Figure 1). It is located in southwestern China (25–40° N, 73–104° E), with an area size of approximately 2.57×10^6 km^2 and an average elevation of >4000 m, characterized by a terrain that slopes from NW to SE and consists of a series of high mountains and plateaus. The mountain ranges primarily include the Himalayas, Kunlun, Tanggula, Qilian, and Hengduan mountains. The plateaus are dominated by the Qiangtang, Qingnan, and the Northwest Sichuan plateaus, inlaid with Qaidam, Qinghai Lake, and other inland basins.

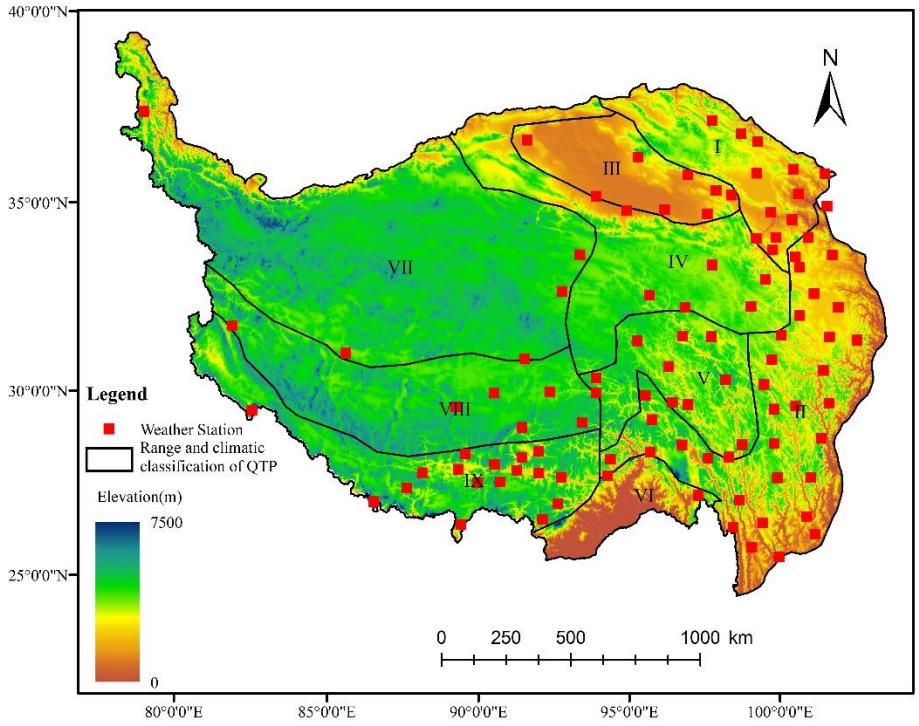

Figure 1. Elevation and the location of nine secondary climate systems of QTP.

QTP has a typical plateau climate system due to its unique topography, with the region's constantly lowest temperature across its latitude. The average annual temperature of QTP is −5.75–2.57 °C, characterized by large daily temperature variability and small annual temperature range. Annual precipitation in most areas of the plateau ranges from 200 to 500 mm, with a decreasing pattern from southeast to northwest and a spatial pattern that is seasonally distributed. The area with the lowest annual precipitation is the NW Qaidam basin, and the highest precipitation levels are seen in the Yarlung Zangbo Grand Canyon area, and the southeast edge of the plateau. Total plateau lake area in the QTP is 3.1 $\times$ 10^4 km^2 which is the reason QTP is also called the 'Water Tower of Asia', as the source of many major rivers, including the Yangtze, Lancang, and Brahmaputra.

Due to the difference of thermal and moisture indices, seven climatic systems are classified as first-level climatic systems in mainland of China by the China Meteorological Administration (CMA). Moreover, according to the topography characteristics and administrative division and differentiation, the first-level climatic systems are divided into 32 secondary sub-systems. The QTP belongs to the plateau climate system (first level) and consists of nine sub-systems (second level), including Qilian-qinghai Lake (I), Bomichuanxi (II), Tsaidam (III), Qingnan (IV), Changdu (V), Dawang-chayu (VI), Zangbei (VII), Zangzhong (VIII) and Zangnan (IX) [9] (Figure 1).

2.2. On-Site Meteorological Data

QTP daily precipitation data for the period of 1981–2014 recorded by 101 meteorological stations were obtained from the China Meteorological Administration (CMA; http://data.cma.cn/) (accessed 20 June 2021). Data quality was strictly controlled by the National Meteorological Information Center of China, whereby data of extreme values and consistency were accepted or rejected upon verification [27]. Locations of the meteorological stations are presented in Figure 1 (geographic coordinates are listed in Appendix A Table A1). Notably, meteorological stations are mainly concentrated in the eastern and southern parts of QTP and are scarce in the northwest region of the plateau.

2.3. Gridded Precipitation Datasets

2.3.1. CMFD

The CMFD was developed by the Institute of Tibetan Plateau Research at the Chinese Academy of Science. It is the first high spatiotemporal resolution meteorological forcing dataset for land process studies in China (http://data.tpdc.ac.cn) (accessed 20 June 2021) [28]. Composite data were derived from the fusion of remote sensing products (GEWEX-SRB, GLDAS, and TRMM 3B42 precipitation datasets), Princeton reanalysis datasets, and in-situ station data at a spatial resolution of 0.1° every three hours, from January 1979 to December 2018. In particular, three background field datasets (TRMM 3B42, GLDAS NOAH10SUBP 3H, and GLDAS NOAH025 3H) were combined to generate the precipitation data. The CMFD dataset was created by using an ANU-Spline interpolation algorithm that takes into account the difference or ratio between the station data and the background field datasets. Owing to its long temporal coverage and high spatial resolution, CMFD has become one of the most widely used meteorological datasets in China [10,29]. The daily precipitation gridded products for 1981–2014 were used in this study.

2.3.2. APHRODITE

APHRODITE's water resources project, in cooperation with the Research Institute for Humanity and Nature (RIHN) of Japan, has compiled a gridded daily product from 1951 to 2015 at a relatively high spatial resolution (0.25° and 0.5°), across the entirety of Asia. The dataset is primarily generated by an improved angular distance-weighting (ADW) method using a dense network of 5000–12,000 rain gauges throughout Asia (http://aphrodite.st.hirosaki-u.ac.jp/) (accessed 20 June 2021) [30]. The interpolation of rain-gauge data to gridded dataset was employed to indicate the ratio of daily precipitation to daily climatology by using a Sphere map scheme that takes into account the daily variation weighting based on the precipitation distribution. For this study, APHRO_MA_V1101 daily precipitation data for 1981–2014 were evaluated at a 0.25° spatial resolution.

2.3.3. CHIRPS

Developed by the UC Santa Barbara Climate Hazards Group, CHIRPS is >35 year old quasi-global rainfall dataset obtained from a combined gauge, satellite, and (re)analysis approach. Its daily datasets span from 1981 to near-present, with a very high spatial resolution (0.05° and 0.25°) and coverage (50° S–50° N, 180° W–180° E; http://chc.ucsb.edu/data/chirps) (accessed 20 June 2021). CHIRPS uses infrared cold cloud duration (CCD) data calibrated with TRMM data to generate the pentadal precipitation estimate, by which the disaggregated data for daily CCD is generated by using the coupled forecast system data with a simple proportional method [31]. In this study, CHIRPS daily precipitation data from 1981 to 2014 were evaluated at a 0.05° resolution.

To analyze the extreme precipitation indices for the QTP region, all three gridded datasets were compared to the observational dataset. Table 1 presents a summary of the three gridded precipitation products used in the present study.

Table 1. Overview of the three gridded precipitation datasets analyzed.

Datasets	Time-Span	Resolution	Data Source(s)	References
CMFD	1979–2018	0.1°/3 h	Gauge, satellite reanalysis	[28]
APHRODITE (APHRO_MA_V1101)	1951–2015	0.25°/daily	Gauge	[30]
CHIRPS	1981–present	0.05°/daily	Gauge, satellite reanalysis	[31]

2.4. Methodology

2.4.1. Extraction of the Gridded Data

To obtain the gridded data from the weather stations, netCDF Operators (NCO), a suite of programs known as 'operators' were used for data interpolation into a specified coordinate point (http://nco.sourceforge.net/) (accessed 20 June 2021). The operators were primarily designed to aid manipulation and analysis of gridded and unstructured data. Data were extracted by using the nearest neighbor algorithm and implemented in the netCDF Kitchen Sink operator.

2.4.2. Index Calculations

A total of 12 extreme precipitation indices were used in this study, as recommended by the Expert Team on Climate Change Detection and Indices [32–34], and they were subsequently categorized into three groups: fixed threshold, station-related threshold, and non-threshold indices [35]. For fixed threshold indices, the number of precipitation occurrences for each index is calculated by a fixed threshold; for example, CWD and R20mm indicate the number of days when precipitation exceeds 1 and 20 mm, respectively. However, for station-related threshold indices, the precipitation values for each site will be different. For instance, the 95th and 99th percentile values of annual precipitation for each station that will vary differently. The non-threshold indices are the last group of extreme indices. There is no need to adopt any thresholds to the data to calculate these indices. Extreme indices such as Rx1day, Rx5day, SDII and PRCPTOT are classified into this group. All 12 indices were calculated by using the *ClimPACT2* software (https://github.com/ARCCSS-extremes/climpact2/) (accessed 20 June 2021), and the details of these extreme precipitation indices are displayed in Table 2. As the four datasets with different temporal resolutions, extreme precipitation indices were computed by arithmetic average method with 101 stations in time series, respectively.

2.4.3. Statistical Analysis

To evaluate the performance of gridded precipitation products in estimating extreme rainfall indices, a point-to-pixel evaluation was carried out at each rain-gauge station in the QTP. Four commonly used metrics, correlation coefficient (CC), root mean square error (RMSE), mean absolute error (MAE), and Kling–Gupa efficiency (KGE score) were adopted for extreme precipitation assessment (Table 3). In addition, three widely used categorical indexes, probability of detection (POD), false alarm ratio (FAR), and critical success index (CSI) were also applied for extreme precipitation event detection.

Based on the formula, the gridded datasets and rain-gauge data are represented by Gi and *Oi*, respectively, where *i* is the index of the station or gridded precipitation data, and n is the total number of stations or gridded precipitation data, *CV* is the coefficient of variation, and bars on variables means the average values. *H* means precipitation event that was detected to occur and observed to occur, and *M* means precipitation event that was not detected to occur but still observed to occur, *F* means precipitation event that was detected to occur but not observed to occur.

Table 2. Precipitation indices used in this study.

	Index	Descriptive Name	Definition	Unit
Fixed threshold indices	CDD	Consecutive dry days	Maximum number of consecutive dry days (when precipitation < 1.0 mm)	day
	CWD	Consecutive wet days	Maximum annual number of consecutive wet days (when precipitation > 1.0 mm)	day
	R10mm	Number of heavy rain days	Number of days when precipitation > 10 mm	day
	R20mm	Number of very heavy rain days	Number of days when precipitation > 20 mm	day
Station-related threshold indices	R95p	Total annual precipitation from heavy rain days	Annual sum of daily precipitation > 95th percentile	mm
	R99p	Total annual precipitation from very heavy rain days	Annual sum of daily precipitation > 99th percentile	mm
	R95pTOT	Contribution from very wet days	100*R95p/PRCPTOT	%
	R99pTOT	Contribution from extremely wet days	100*R99p/PRCPTOT	%
Non-threshold indices	PRCPTOT	Annual total wet day precipitation	Sum of daily precipitation > 1.0 mm	mm
	Rx1day	Maximum 1-day precipitation	Maximum 1-day precipitation total	mm
	Rx5day	Maximum 5-day precipitation	Maximum 5-day precipitation total	mm
	SDII	Daily precipitation n intensity	Annual total precipitation divided by the number of wet days (when total PR > 1.0 mm)	mm/day

Table 3. Statistical metrics used in the study.

Statistics	Formula	Value Range	Perfect Value
Correlation coefficient (CC)	$CC = \frac{\sum(G_i-\overline{G})(O_i-\overline{O})}{\sqrt{\sum(G_i-\overline{G})^2\sum(O_i-\overline{G})^2}}$	$[-1, 1]$	1
Root mean square error (RMSE)	$RMSE = \sqrt{\frac{1}{n}\sum_{i=1}^{n}(O_i - G_i)^2}$	$[0, +\infty)$	0
Mean absolute error (MAE)	$MAE = \frac{1}{n}\sum_{i=1}^{n}\lvert P_i - O_i\rvert$	$[0, +\infty)$	0
KGE score	$1 - \sqrt{(CC-1)^2 + (x-1)^2 + (y-1)^2}$ where x = $\overline{G}/\overline{O}$, y = CV_G/CV_O	$(-\infty,1]$	1
The probability of detection (POD)	$POD = \frac{H}{H+M}$	[0, 1]	1
The ratio false alarm (FAR)	$FAR = \frac{F}{H+F}$	[0, 1]	0
Critical success index (CSI)	$CSI = \frac{H}{H+M+F}$	[0, 1]	1

3. Results

3.1. Spatial Evaluation

Initial result analyses were performed to examine the alignment between the indices of extreme rainfall and the gauge-based data, of which Taylor diagrams corresponding to the 12 matched groups are presented below.

3.1.1. Fixed Threshold Indices

Figure 2 presents the performance of the four datasets—gauges (OBS), CMFD, APHRODITE, and CHIRPS—in capturing the fixed threshold indices consecutive dry days (daily precipitation < 1 mm, CDD), consecutive wet days (daily precipitation $\geq$ 1 mm, CWD), number of days with precipitation $\geq$ 10 mm (R10mm), and number of days with precipitation $\geq$ 20 mm (R20mm).

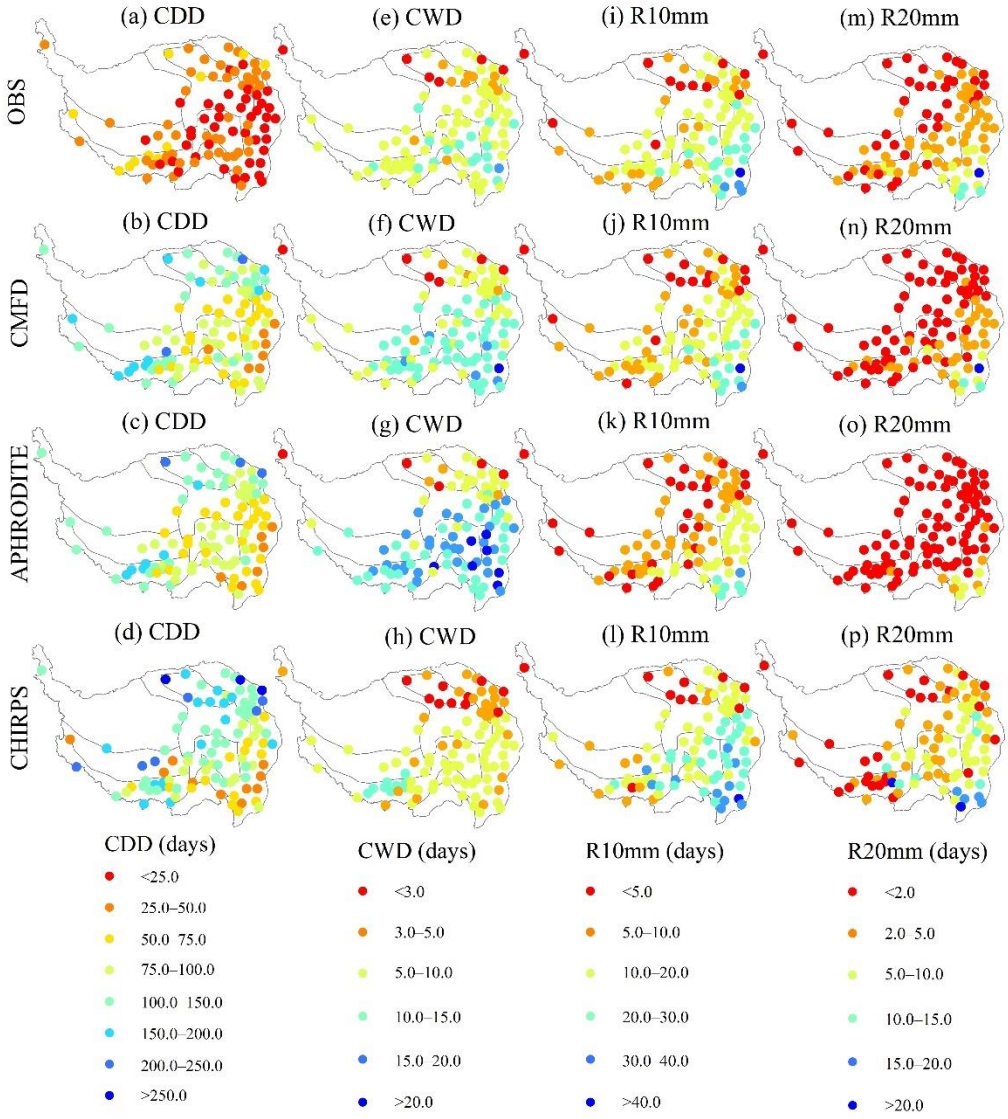

Figure 2. Mean spatial distribution of fixed threshold indices from 1981 to 2014: CDD, CWD, R10mm, and R20mm.

Generally, the three gridded products showed variable spatial distribution, and overestimated CDD (Figure 2a–d) with correlation coefficients of 0.85, 0.78, and 0.37, RMSE values of 27.55, 31.86, and 56.56 days, MAE values of 16.69, 20.68, and 54.12 days, and KGE scores of 0.82, 0.77, and 0.30 for CMFD, APHRODITE, and CHIRPS, respectively (Figure 3a, Figure 4, Appendix A Table A2). Spatial patterns of CC for CDD are shown in Figure 5a–c, and the findings suggested that CMFD was the most accurate dataset examined. Spatial patterns of RMSE and MAE for CDD are shown in Figures 6a–c and 7a–c. The RMSE and MAE values of CHIRPS were significantly larger than that of the other indices, and with lower accuracy in the southern and northern parts of QTP for all three datasets.

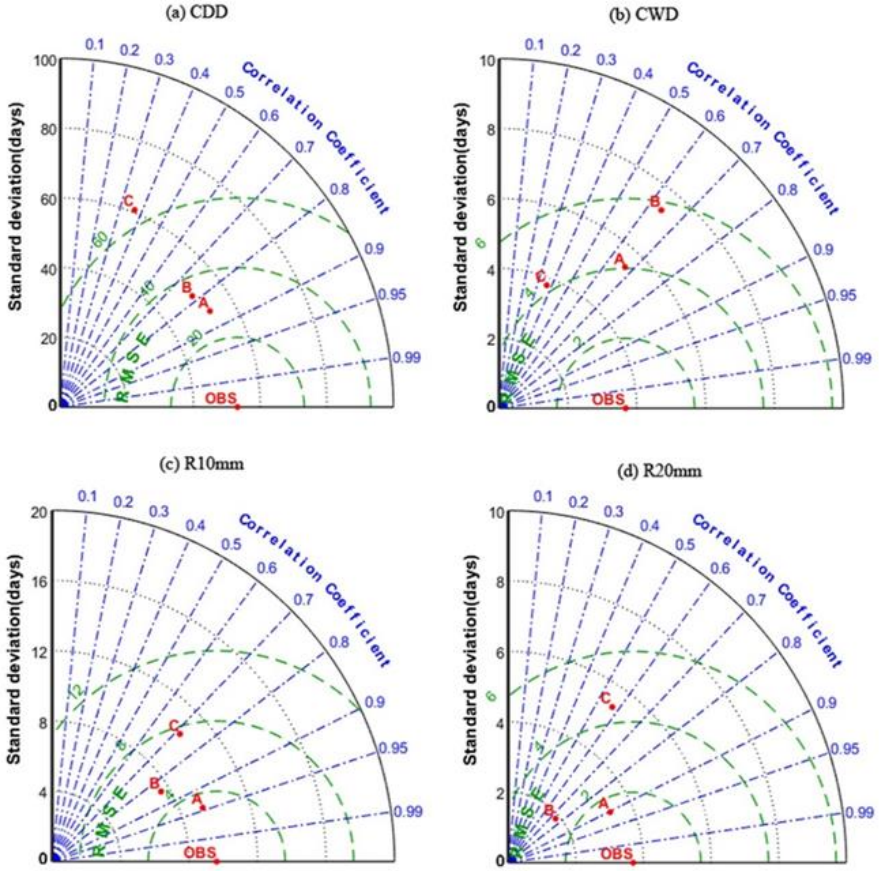

Figure 3. Taylor diagrams indicating correlation coefficients, standard deviation, and RMSE of CDD, CWD, R10mm, and R20mm indices from 1981 to 2014. (A) CMFD, (B) APHRODITE, and (C) CHIRPS. The radial coordinate (y axis) represents the magnitude of standard deviation, concentric semicircles represent RMSE, and the angular coordinate represents the correlation coefficient.

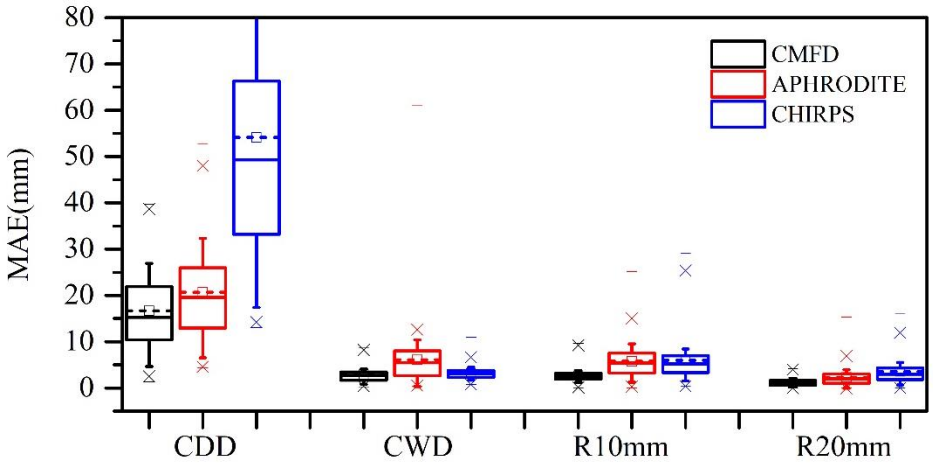

Figure 4. Boxplots of the mean absolute error (MAE) for gauge-based fixed threshold indices CDD, CWD, R10mm, and R20mm, as derived from CMFD, APHRODITE, and CHIRPS at 101 rain-gauges. Five lines from bottom to top for one box represent minimum value, 25th percentile, 50th percentile, 75th percentile, and maximum value, respectively. The quadrate inside the box represents the mean values. The asterisks represent several possible alternative values.

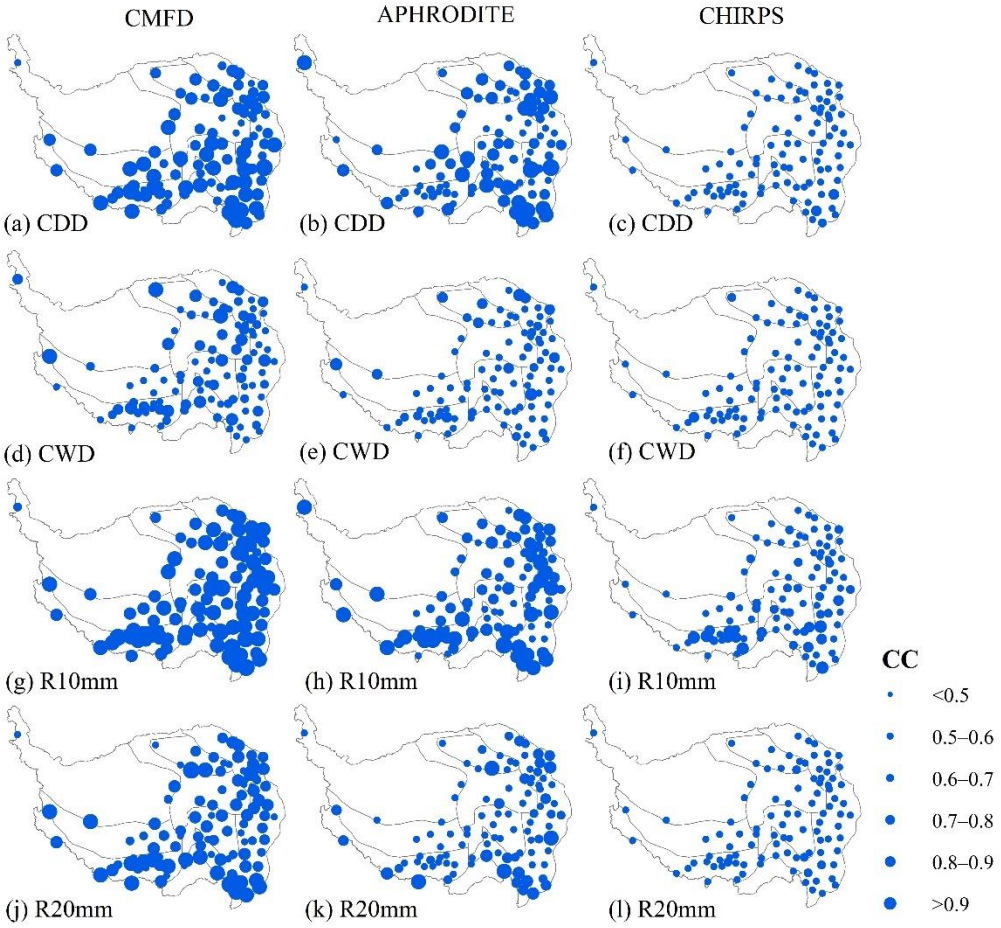

Figure 5. Correlations between gauge-based fixed threshold indices CDD, CWD, R10mm, and R20mm, as derived from CMFD, APHRODITE, and CHIRPS for the period 1981–2014.

CWD analyses indicated that all three products failed to accurately capture this pattern (Figure 2e–h, Figure 5d–f). In general, CMFD and APHRODITE overestimated CWD over the entire QTP, whereas CHIRPS underestimated this index. The correlation coefficients were 0.67, 0.64, and 0.38, RMSE values were 4.04, 5.67, and 3.52 days, MAE values were 2.87, 6.07, and 3.17 days, and KGE scores were 0.53, 0.21, and 0.31 for CMFD, APHRODITE, and CHIRPS, respectively (Figure 3b, Figure 4, Appendix A Table A2). Spatial patterns of RMSE and MAE for CWD are displayed in Figures 6d–f and 7d–f. Contrary to CC, the RMSE and MAE values of CHIRPS were the lowest among the three datasets.

Analysis of R10mm suggested that the three products were of equal performance (Figure 2i–l). Both CMFD and APHRODITE slightly underestimated R10mm across all stations, whereas CHIRPS tended to overestimate this index. The correlation coefficients were 0.94, 0.85, and 0.72, RMSE values were 3.07, 3.99, and 7.26 days, MAE values were 2.69, 5.79, and 5.99 days, and KGE scores were 0.81, 0.49, and 0.54 for CMFD, APHRODITE, and CHIRPS, respectively (Figure 3c, Figure 4, Appendix A Table A2). CC spatial patterns for R10mm are shown in Figure 5g–i, and spatial patterns of RMSE and MAE values are shown in Figures 6g–i and 7g–i. Observed errors were larger in Bomi-chuanxi (II) and Dawang-chayu (VI) based on APHRODITE and CHIRPS.

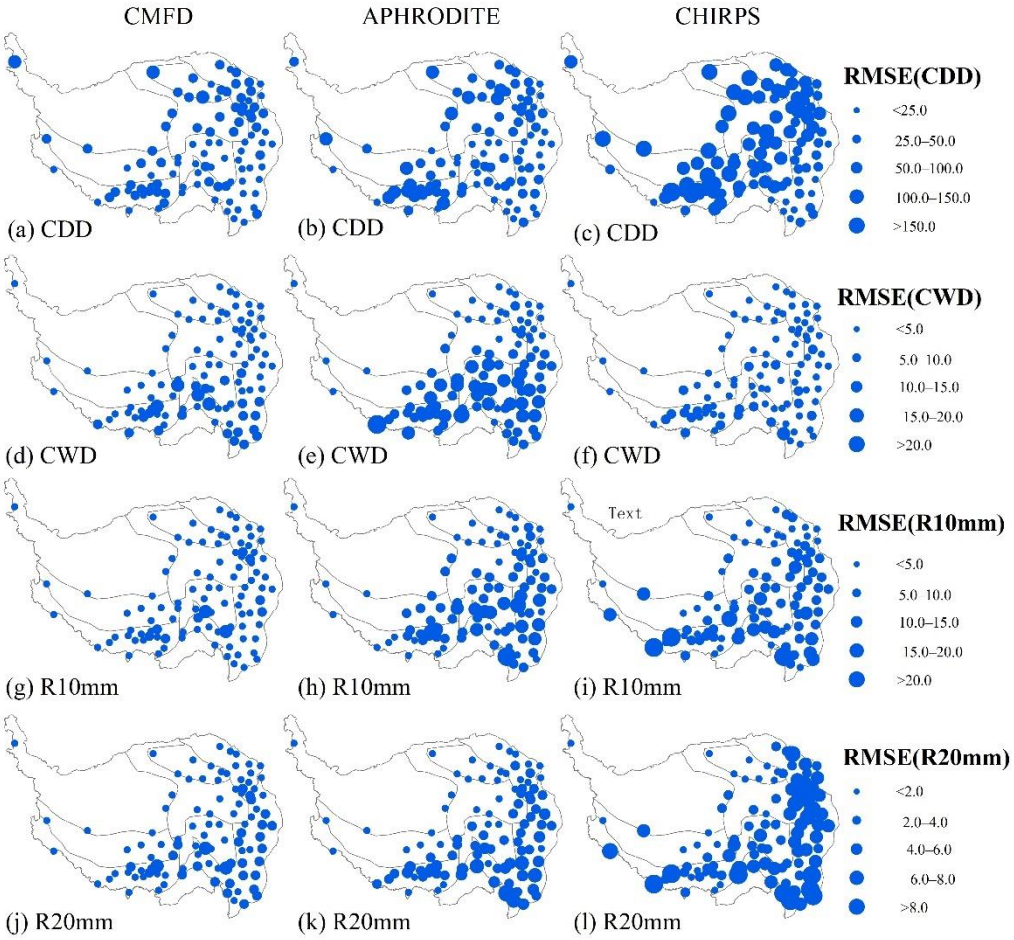

Figure 6. RMSE for gauge-based fixed threshold indices CDD, CWD, R10mm, and R20mm, as derived from CMFD, APHRODITE, and CHIRPS for the period 1981–2014.

The R20mm findings suggested that the spatial values derived from the three gridded products were in accordance with OBS data (Figure 2m–p). Correlation coefficients were 0.90, 0.75, and 0.57, RMSE values were 1.44, 1.25, and 4.42 days, MAE values were 1.19, 2.32, and 3.55 days, and KGE scores were 0.59, 0.36, and 0.22 for CMFD, APHRODITE, and CHIRPS, respectively (Figure 3d, Figure 4, Appendix A Table A2). Spatial patterns of CC, RMSE and MAE are displayed in Figure 5j–l, Figures 6j–l and 7j–l, respectively. CMFD and APHRODITE performed similarly well when assessing this index.

3.1.2. Station-Related Threshold Indices

The mean spatial distribution of four station-related threshold indices including the annual sum of daily precipitation >95th percentile (R95p), >99th percentile (R99p), contribution from very wet days (R95pTOT), and contribution from extremely wet days (R99pTOT) are displayed in Figure 8. Spatial agreement analysis further revealed that the four indices were in accordance with OBS data; however, CMFD and APHRODITE slightly underestimated these indices in most of the QTP, and CHIRPS indices were overestimated for the entirety of the region analyzed.

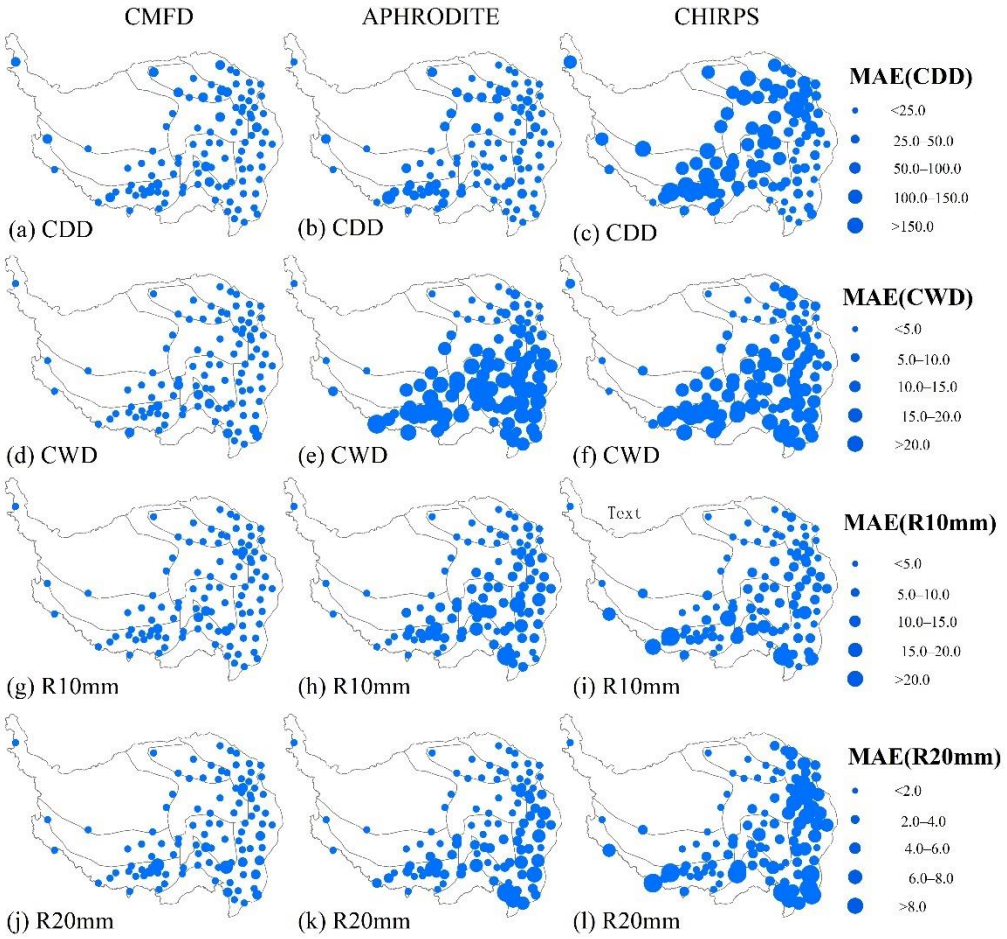

Figure 7. MAE for gauge-based fixed threshold indices CDD, CWD, R10mm, and R20mm, as derived from CMFD, APHRODITE, and CHIRPS for the period 1981–2014.

Index results for R95p are displayed in Figure 9a, Figure 10, and Appendix A Table A2. Correlation coefficients were 0.88, 0.77, and 0.46, RMSE values of 37.19, 40.63, and 73.47 mm, MAE values of 25.87, 35.05, and 59.56 mm, and KGE scores of 0.87, 0.72, and 0.46 for CMFD, APHRODITE, and CHIRPS, respectively. Spatial patterns of CC for R95p are shown in Figure 11a–c, indicating that CMFD had consistently maintained the highest levels of accuracy, followed by APHRODITE and CHIRPS. Spatial patterns of RMSE and MAE are shown in Figures 12a–c and 13a–c, indicating that the RMSE and MAE values of CMFD were the smallest, followed by those of APHRODITE and CHIRPS.

Results for the indexes of R99p, R95PTOT, and R99PTOT are displayed in Figure 8b–d, indicating that the three products could not be used to depict the indices accurately. Correlation coefficients for R99p, R95PTOT, and R99PTOT were <0.73, 0.73, 0.64, for CMFD, APHRODITE, and CHIRPS, respectively (Figure 9d–l). CMFD and APHRODITE accounted for 70% of the total stations where the CC values were lower than 0.7. Additionally, CC values of the 101 stations were all lower than 0.7 for CHIRPS. Spatial patterns of RMSE and MAE values for R99p, R95PTOT, and R99PTOT are shown in Figures 10d–l and 11d–l, indicating again that CMFD was the most accurate, followed by APHRODITE and CHIRPS; errors for all three datasets peaked for the Zangnan (IX), Dawang-chayu (VI) and Qinlian-Qinghai Lake (I) of the QTP.

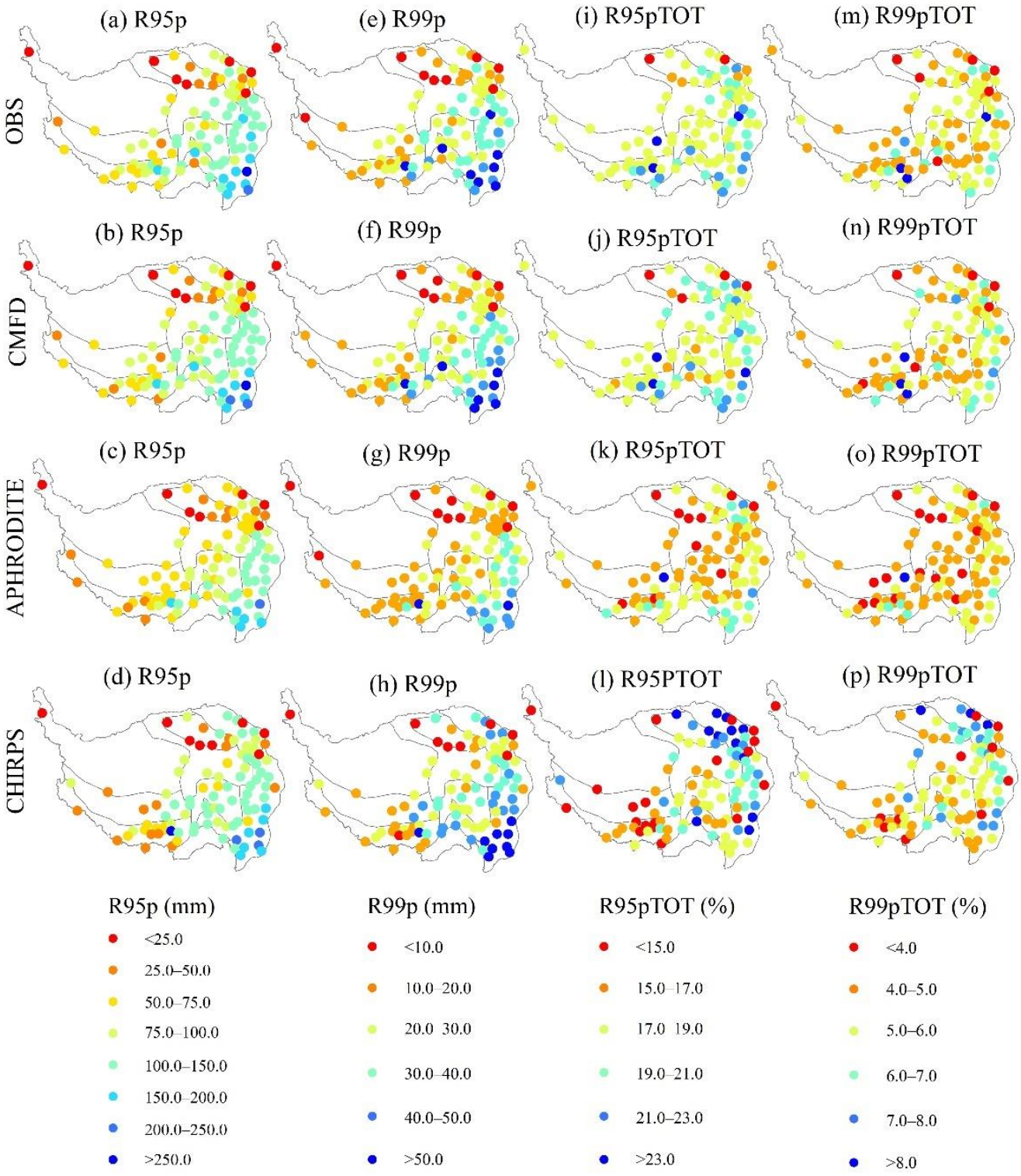

Figure 8. Mean spatial distribution of station-related threshold indices from 1981 to 2014: R95p, R99p, R95pTOT, and R99pTOT.

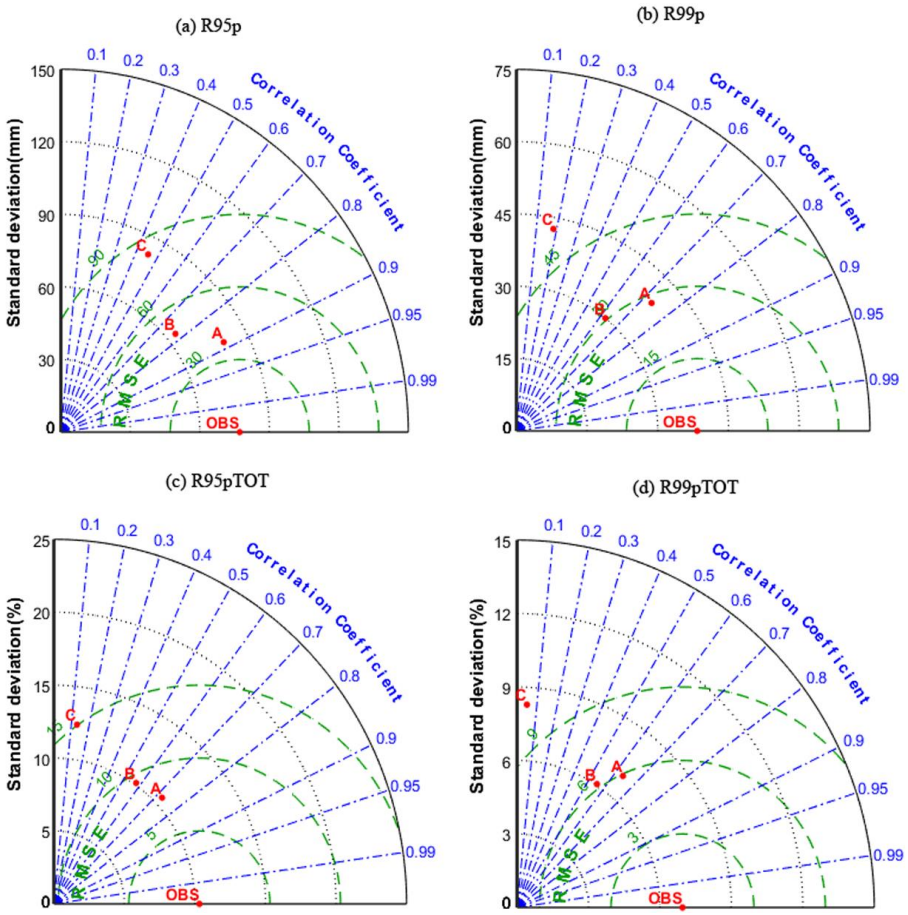

Figure 9. Taylor diagrams indicating correlation coefficients, standard deviation, and RMSE of R95p, R99p, R95pTOT, and R99pTOT indices from 1981 to 2014. (A) CMFD, (B) APHRODITE, and (C) CHIRPS. The radial coordinate (y axis) represents the magnitude of standard deviation, concentric semicircles represent RMSE, and the angular coordinate represents the correlation coefficient.

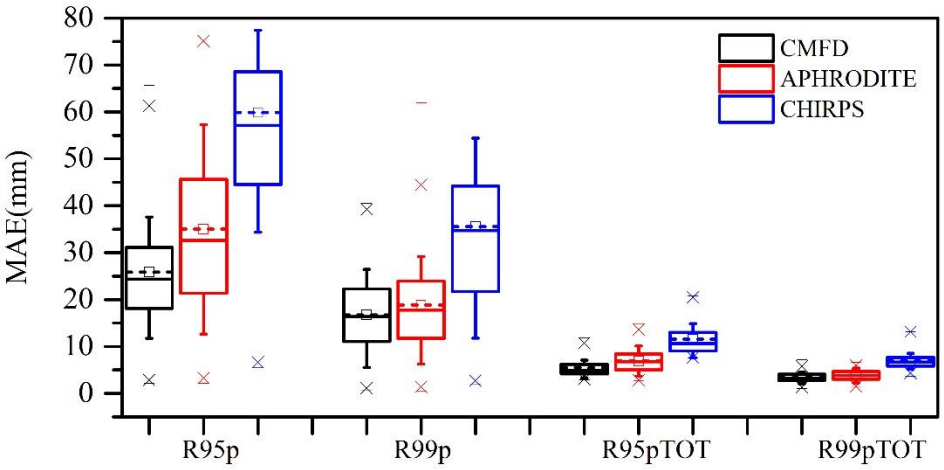

Figure 10. Boxplots of the mean absolute error (MAE) for gauge-based station threshold indices R95p, R99p, R95pTOT, and R99pTOT, as derived from CMFD, APHRODITE, and CHIRPS at 101 rain gauges. Five lines from bottom to top for one box represent minimum value, 25th percentile, 50th percentile, 75th percentile, and maximum value, respectively. The quadrate inside the box represents the mean values. The asterisks represent several possible alternative values.

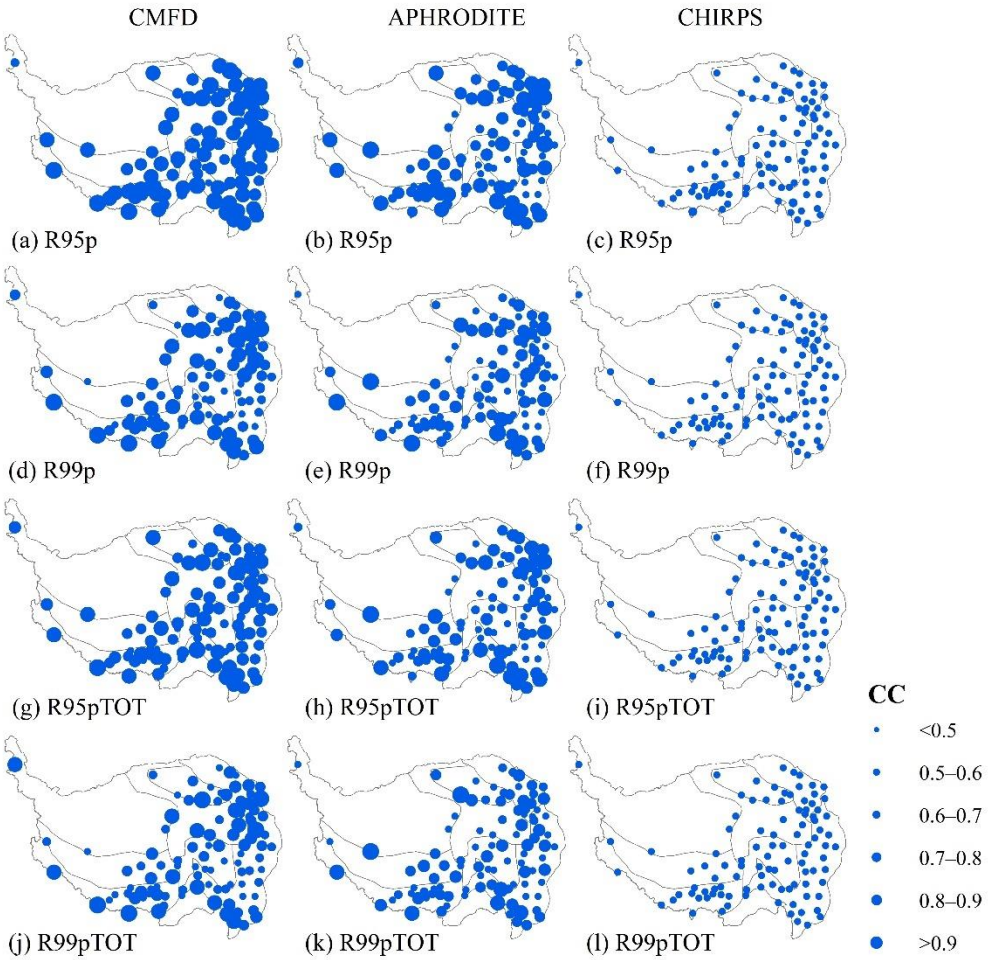

Figure 11. Correlations between gauge-based station threshold indices R95p, R99p, R95pTOT, and R99pTOT, as derived from CMFD, APHRODITE, and CHIRPS for the period 1981–2014.

3.1.3. Non-Threshold Indices

The mean spatial distribution of the four non-threshold indices, including total precipitation (PRCPTOT), maximum annual one day precipitation (Rx1day), maximum annual 5-day precipitation (Rx5day), and simple daily intensity index (SDII), are displayed in Figure 14.

Analysis of PRCPTOT revealed the variability among the three gridded products (Figure 14a–d). Both CMFD and APHRODITE datasets underestimated PRCPTOT at stations 85 and 86, respectively, with an average underestimation of 15.92 and 55.42 mm, respectively. CHIRPS overestimated this index for 70 of the 101 stations with an average value of 93.76 mm. Correlation coefficients were 0.98, 0.95, and 0.78, RMSE values were 50.2, 68.53, and 167.17 mm, MAE values were 25.41, 60.28, and 108.33 mm, and KGE scores were 0.97, 0.87, and 0.75 for CMFD, APHRODITE, and CHIRPS, respectively (Figure 15a, Figure 16 and Appendix A Table A2). Spatial patterns of CC, RMSE and MAE for PRCPTOT can be seen in Figure 17a–c, Figures 18a–c and 19a–c, respectively, demonstrating that all three gridded products predicted this index well. RMSE and MAE values of CHIRPS were larger than that of the other two datasets, and the accuracy of all three datasets was lowest in the Zangnan (IX) and Dawang-chayu (VI) of the QTP.

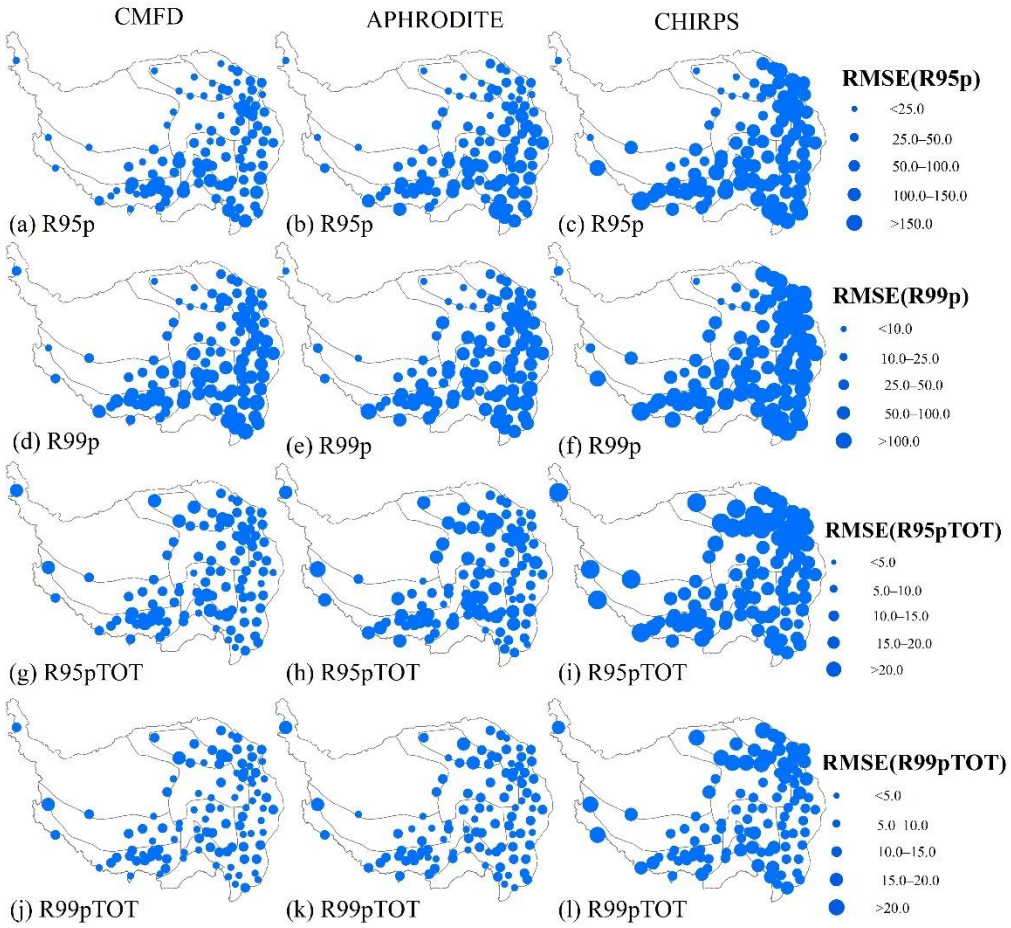

Figure 12. RMSE for gauge-based station threshold indices R95p, R99p, R95pTOT, and R99pTOT as derived from CMFD, APHRODITE, and CHIRPS for the period 1981–2014.

Analysis of Rx1day highlighted the different patterns of each gridded product (Figure 14e–h). In general, CMFD and APHRODITE underestimated Rx1day over the entire QTP by an average amount of 3.23 and 10.35 mm, respectively; whereas CHIRPS overestimated the index by an average value of 16.90 mm. Correlation coefficients were 0.88, 0.77, and 0.51, RMSE values were 6.37, 5.60, and 18.34 mm, MAE values were 5.08, 10.38, and 17.71 mm, KGE scores were 0.53, 0.21, and 0.31 for CMFD, APHRODITE, and CHIRPS, respectively (Figure 15b, Figure 16 and Appendix A Table A2). Spatial patterns of CC are shown in Figure 17d–f, indicating that CMFD outperformed the other indices. Spatial patterns of RMSE and MAE for Rx1day are shown in Figures 18d–f and 19d–f and are identical to the patterns of CCs. The overall accuracy was lowest in the Qilian-qinghai Lake (I) and Bomi-chuanxi (II) of the QTP for all three products.

The spatial patterns of Rx5day are displayed in Figure 14i–l, indicating results that are similar to Rx1day, whereas CMFD and APHRODITE underestimated index values by 3.56 and 13.98 mm, respectively, and CHIRPS overestimated them by 17.97 mm. Correlation coefficients were 0.95, 0.87, and 0.61, RMSE values were 8.99, 9.77, and 27.40 mm, MAE values were 6.14, 14.43, and 21.19 mm, KGE scores were 0.92, 0.72, and 0.56 for CMFD, APHRODITE, and CHIRPS, respectively (Figure 15c, Figure 16 and Appendix A Table A2). Spatial patterns of CC for Rx5day are displayed in Figure 17g–i, RMSE and MAE patterns are displayed in Figures 18g–i and 19g–i .

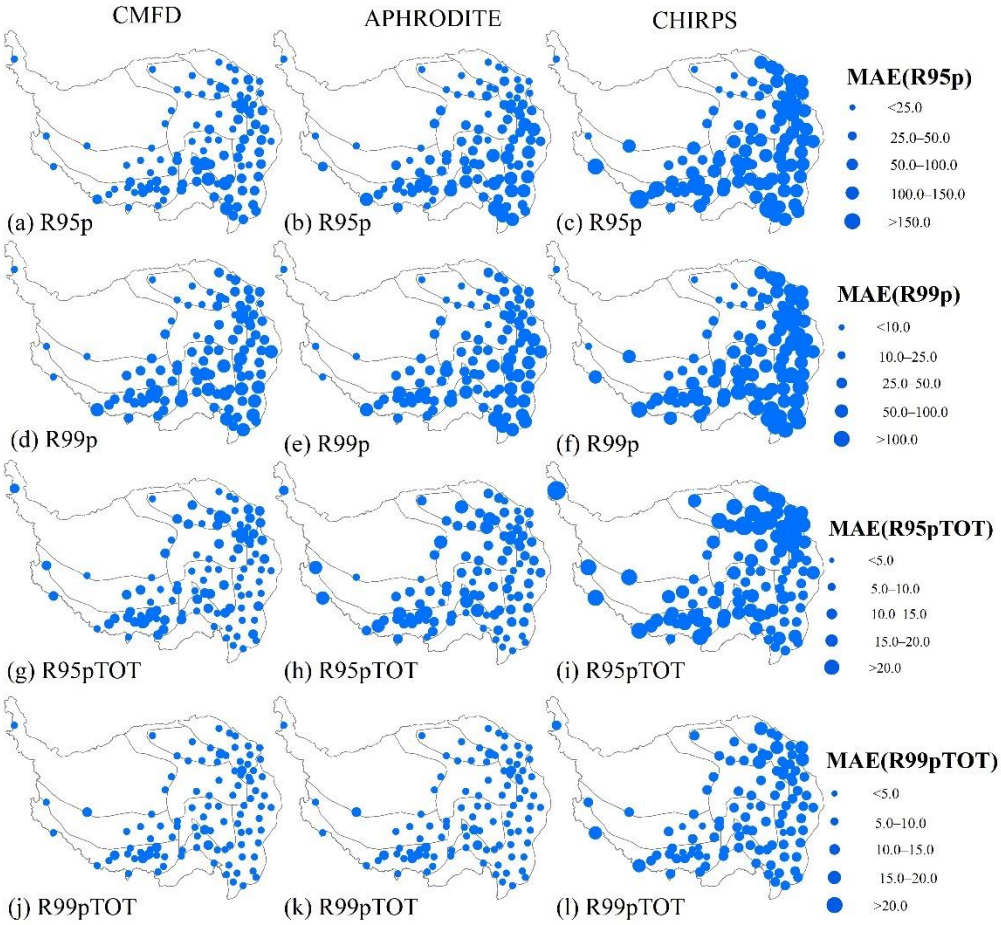

Figure 13. MAE for gauge-based station threshold indices R95p, R99p, R95pTOT, and R99pTOT as derived from CMFD, APHRODITE, and CHIRPS for the period 1981–2014.

Spatial distribution of SDII can be seen in Figure 14m–p, indicating that both CMFD and APHRODITE yielded slightly underestimated results by an average of 0.82 and 1.61 mm/day, respectively. CHIRPS showed a pattern of strong overestimation for SDII, by an average value of 3.87 mm/day. Correlation coefficients were 0.89, 0.80, and 0.58, RMSE values were 0.62, 0.62, and 2.75 mm, MAE values were 0.85, 1.62, and 3.80 mm, KGE scores were 0.82, 0.67, and 0.46 for CMFD, APHRODITE, and CHIRPS, respectively (Figure 15d, Figure 16 and Appendix A Table A2). Spatial patterns of CC, RMSE, and MAE for SDII indicated that CMFD and APHRODITE outperformed CHIRPS (Figure 17j–l, Figures 18j–l and 19j–l).

3.2. Temporal Evaluation

The second overarching question addressed was the temporal agreement between the three gridded and OBS datasets across the entire study area. Accordingly, annual time series were generated for each of the four datasets over the study area. Figure 20 shows the mean annual rainfall indices for all 101 rain-gauge stations in the QTP.

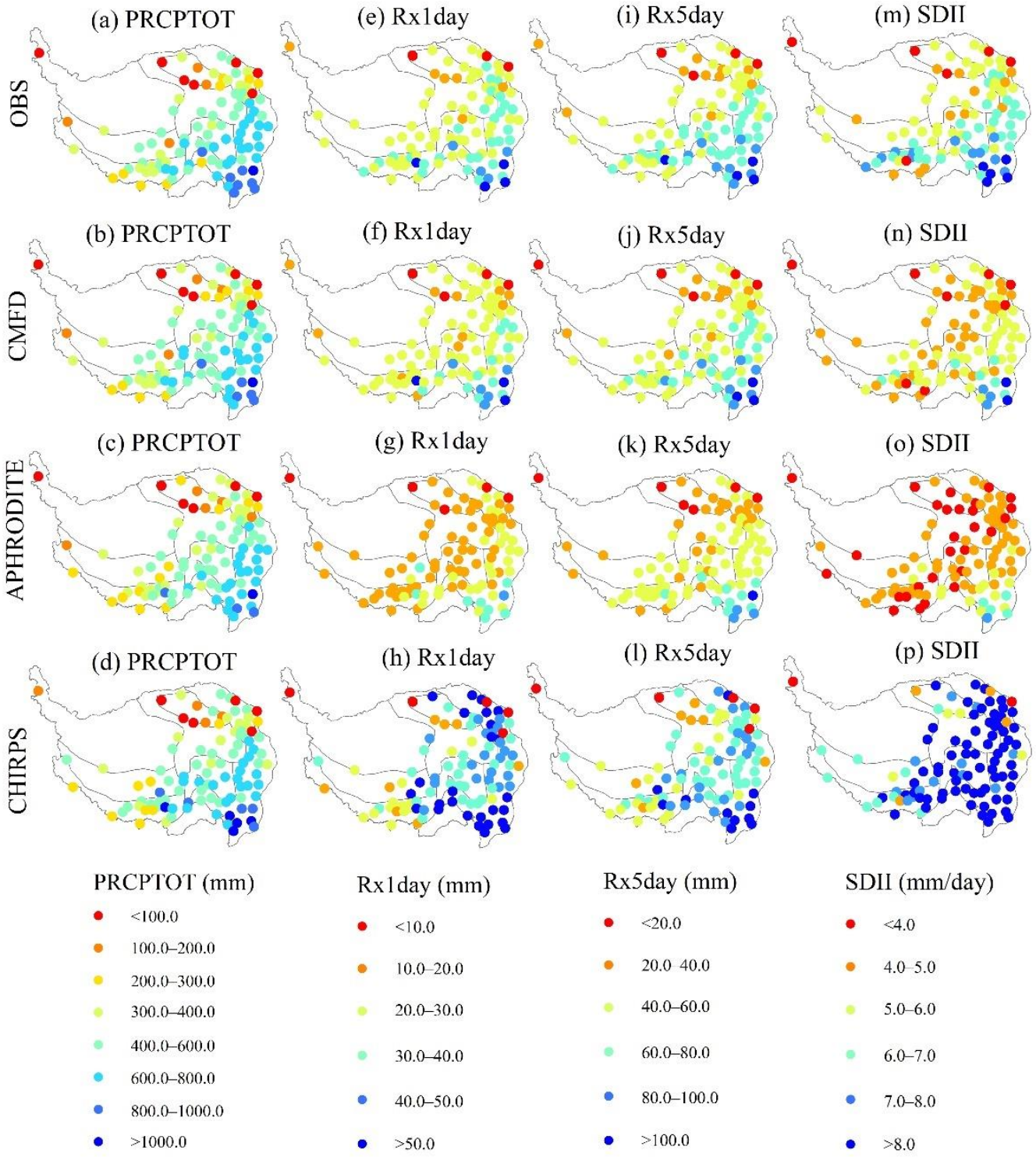

Figure 14. Mean spatial distribution of non-threshold indices from 1981–2014: PRCPTOT, Rx1day, Rx5day, and SDII.

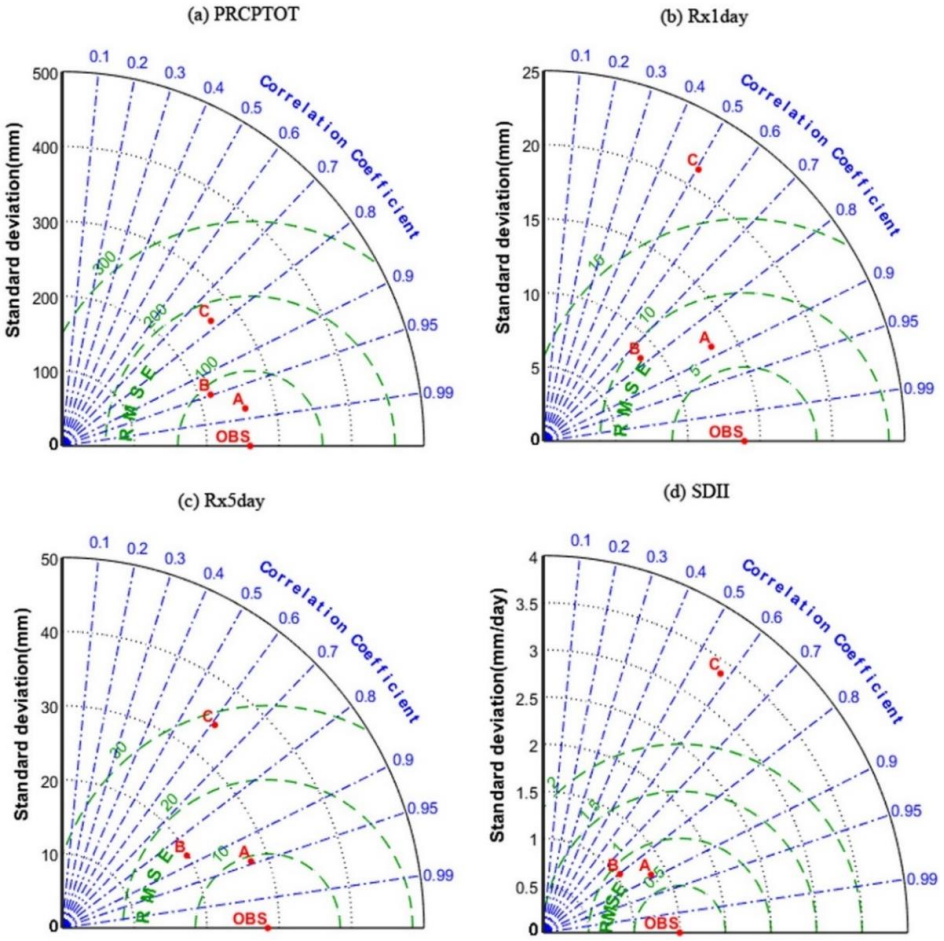

Figure 15. Taylor diagrams indicating correlation coefficients, standard deviation, and RMSE of PRCPTOT, Rx1day, Rx5day, and SDII indices from 1981 to 2014. (A) CMFD, (B) APHRODITE, and (C) CHIRPS. The radial coordinate (y axis) represents the magnitude of standard deviation, concentric semicircles represent RMSE, and the angular coordinate represents the correlation coefficient.

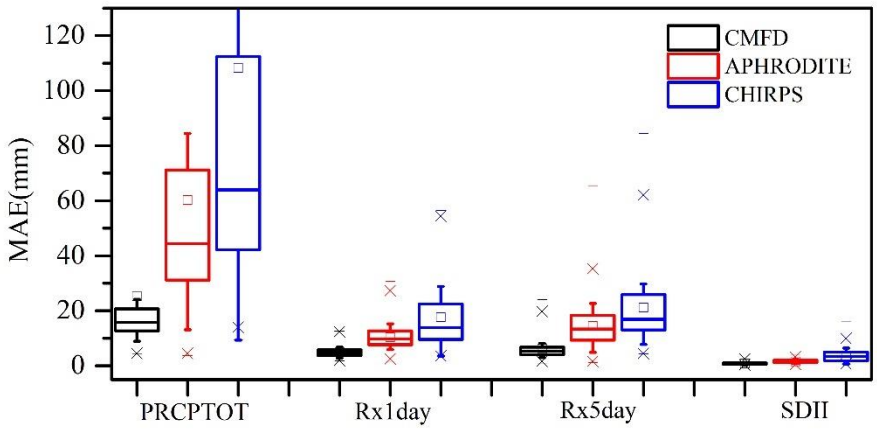

Figure 16. Boxplots of the mean absolute error (MAE) for gauge-based non-threshold indices PRCPTOT, Rx1day, Rx5day, and SDII, as derived from CMFD, APHRODITE, and CHIRPS at 101 rain gauges. Five lines from bottom to top for one box represent minimum value, 25th percentile, 50th percentile, 75th percentile, and maximum value, respectively. The quadrate inside the box represents the mean values. The asterisks represent several possible alternative values.

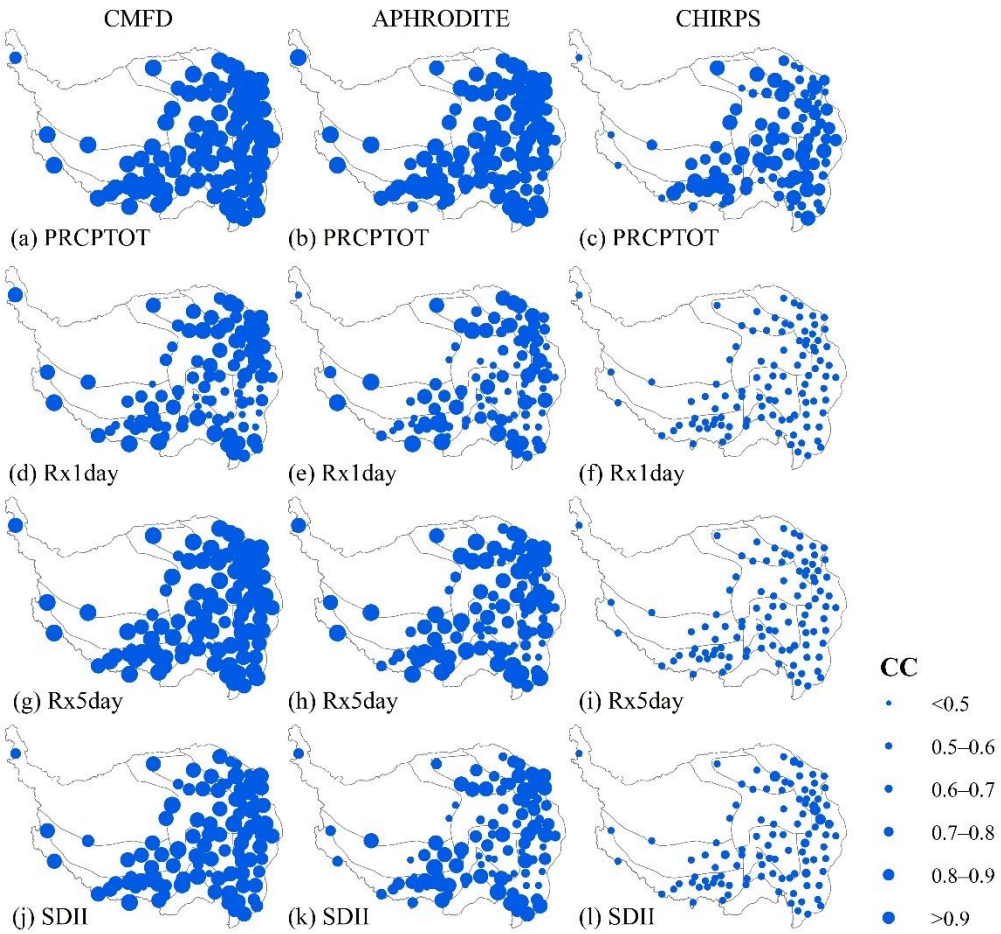

Figure 17. Correlations between gauge-based non-threshold indices PRCPTOT, Rx1day, Rx5day, and SDII, as derived from CMFD, APHRODITE, and CHIRPS from 1981 to 2014.

CMFD produced the most accurate results for PRCPTOT, while both CMFD and APHRODITE overestimated the CWD, and underestimated R10mm, R20mm, Rx1day, Rx5day, PRCPTOT, and SDII. CHIRPS underestimated CWD and overestimated the extreme rainfall indices for R10mm, R20mm, Rx1day, Rx5day, PRCPTOT, and SDII.

The values of CC and RMSE for the time series of the three gridded datasets are shown in Table 4. Spatial analysis revealed that the strongest correlations were with PRCPTOT, at CC values of 0.96, 0.93, and 0.78, for CMFD, APHRODITE, and CHIRPS, respectively. CC of CMFD were >0.70 for 10 of the 12 indices of extreme rainfall examined; while 8 of the 12 indices of APHRODITE, and only 2 of the 12 indices of CHIRPS met the same criterions. The RMSE values of CMFD were the smallest for all indices except CWD, where those of CHIRPS were the highest among the three datasets, suggesting that CMFD is a superior time-series evaluation metric for extreme rainfall in the QTP.

3.3. Detection Capabilities and Precipitation Intensities Analysis

The results of three gridded products in detecting general rain events (with daily precipitation amount < 20 mm) and heavy and extreme rain events (with daily precipitation amount $\geq$ 20 mm) are shown in Figure 21 and Appendix A Table A3. Overall, the performance of CMFD is better than that of APHRODITE and CHIRPS. For general rain events, both CMFD and APHRODITE performed similarly well, with high POD values of 0.93, and 0.95, and low FAR values of 0.31, and 0.38, respectively (Figure 21a–c). It indicated that CMFD and APHRODITE detected general rain events well among the three products. In addition, CSI represented similar results with POD. For heavy and extreme rain events, POD and CSI values were much lower, POD values were at 0.49, 0.17, and

0.10, and CSI values were at 0.42, 0.15, and 0.03 for CMFD, APHRODITE, and CHIRPS, respectively (Figure 21d–f). Low POD and CSI values and High FAR values indicated that the abilities of three gridded products to detect the heavy and extreme precipitation thresholds were still low and need to be improved.

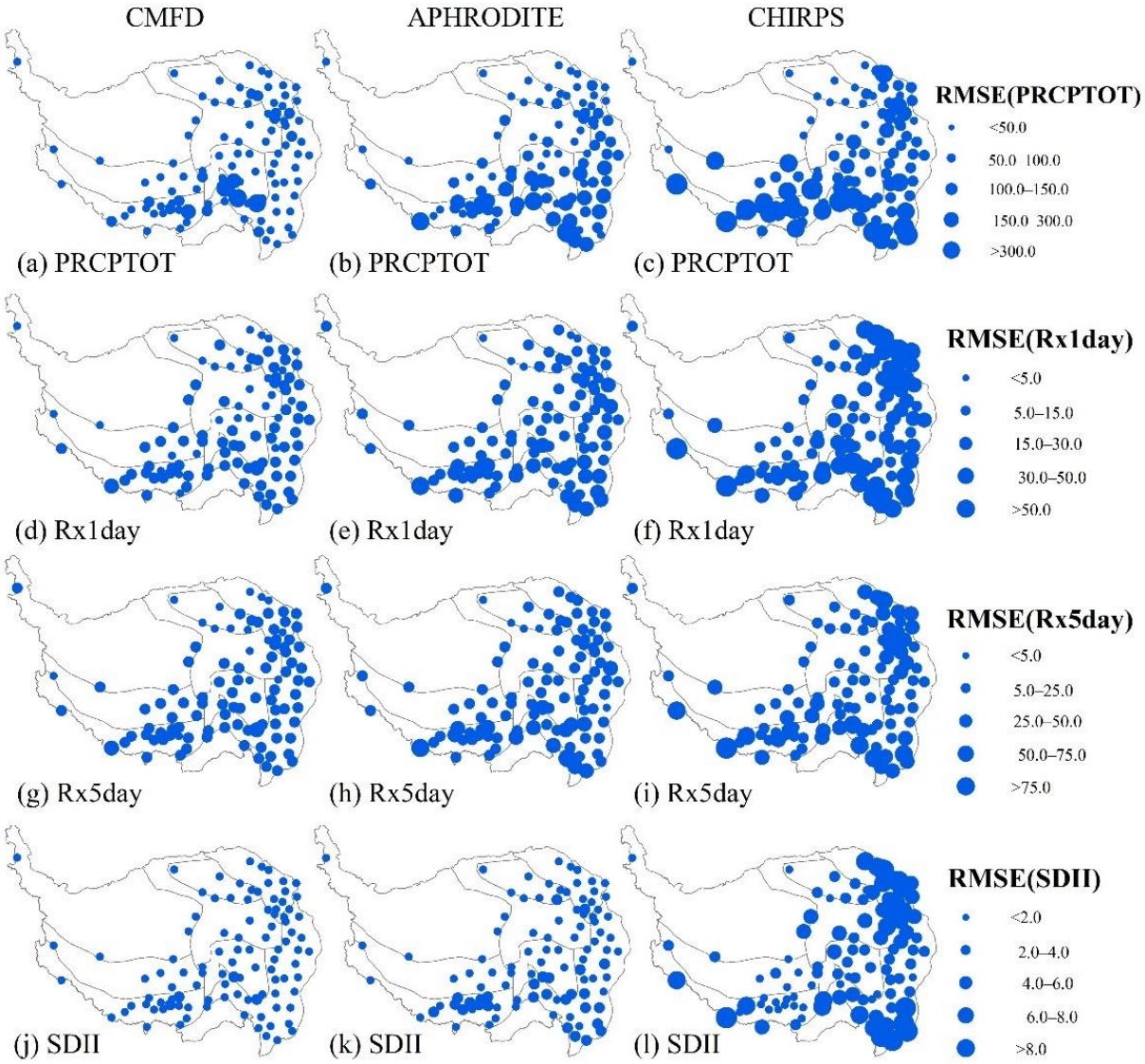

Figure 18. RMSE for gauge-based non-threshold indices PRCPTOT, Rx1day, Rx5day, and SDII as derived from CMFD, APHRODITE, and CHIRPS from 1981 to 2014.

Table 4. Time series of annual extreme rainfall indices based on CMFD, APHRODITE, and CHIRPS. datasets from 1981 to 2014.

Index	Unit	CC			RMSE		
		CMFD	APHRODITE	CHIRPS	CMFD	APHRODITE	CHIRPS
CDD	day	0.85	0.77	0.36	28.84	34.16	69.41
CWD	day	0.69	0.50	0.37	4.50	10.15	4.36
R10mm	day	0.94	0.85	0.72	3.72	7.54	8.24
R20mm	day	0.90	0.74	0.58	1.82	3.44	5.06
R95p	mm	0.89	0.77	0.46	37.24	51.16	82.90
R99p	mm	0.73	0.62	0.16	27.61	30.48	54.10
R95pTOT	%	0.73	0.57	0.13	7.66	9.55	15.01
R99pTOT	%	0.63	0.54	0.06	5.80	6.12	10.45
PRCPTOT	mm	0.96	0.93	0.78	49.50	95.95	178.78
Rx1day	mm	0.88	0.77	0.46	7.37	13.41	25.85
Rx5day	mm	0.95	0.87	0.61	9.61	19.89	29.97
SDII	mm/day	0.90	0.80	0.54	1.05	1.83	4.84

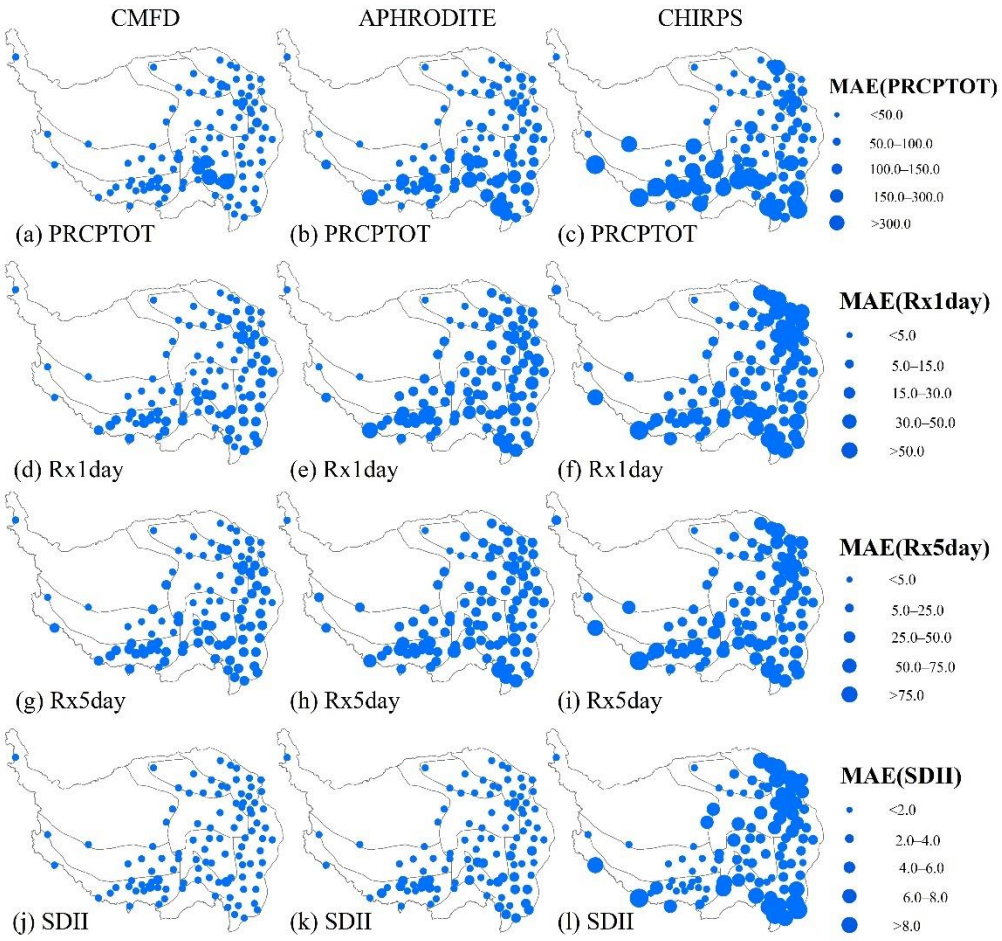

Figure 19. MAE for gauge-based non-threshold indices PRCPTOT, Rx1day, Rx5day, and SDII as derived from CMFD, APHRODITE, and CHIRPS from 1981 to 2014.

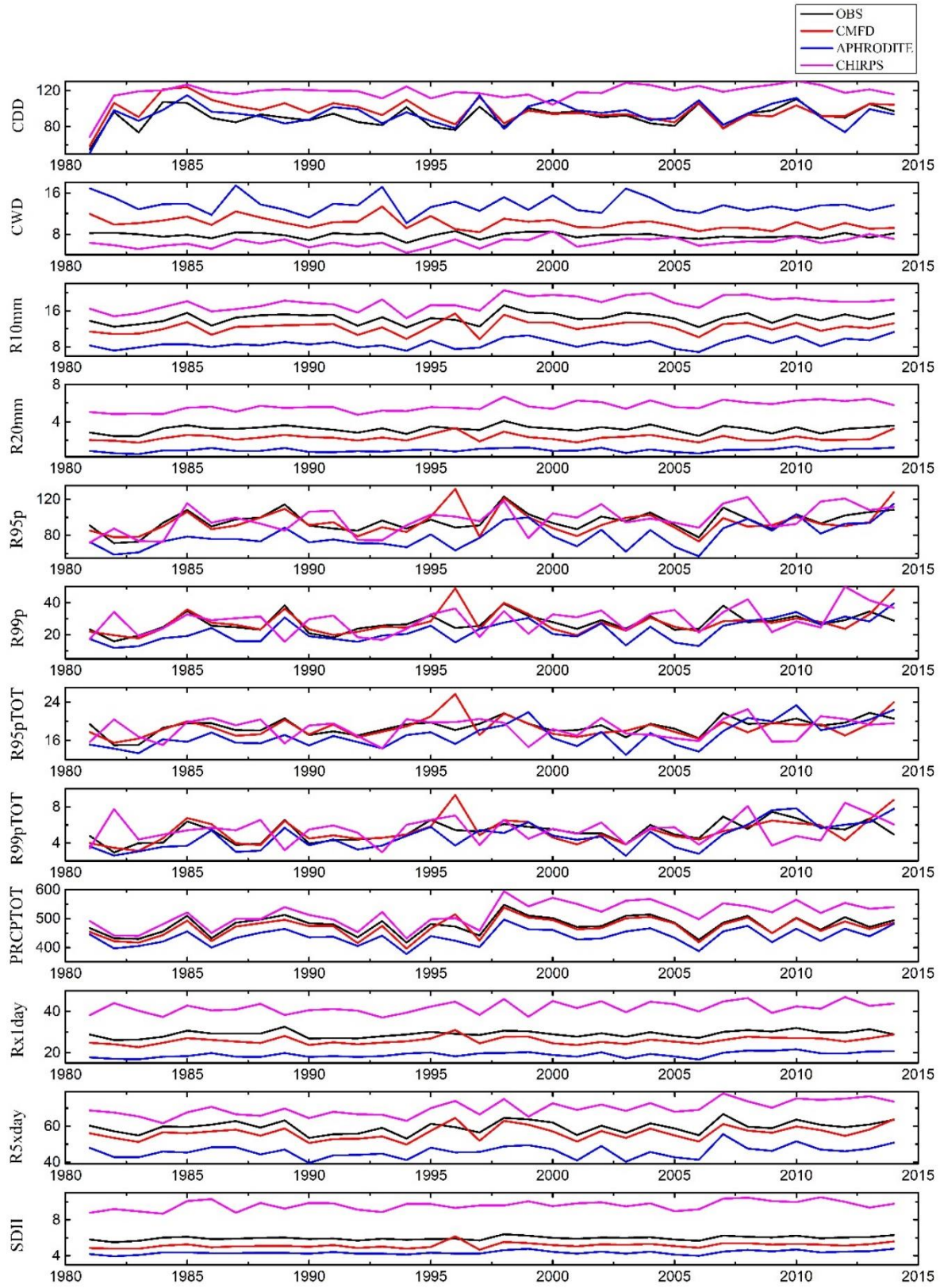

Figure 20. Mean annual rainfall indices of the 101 rain-gauge stations, and the corresponding CMFD, APHRODITE, and CHIRPS estimates from 1981 to 2014.

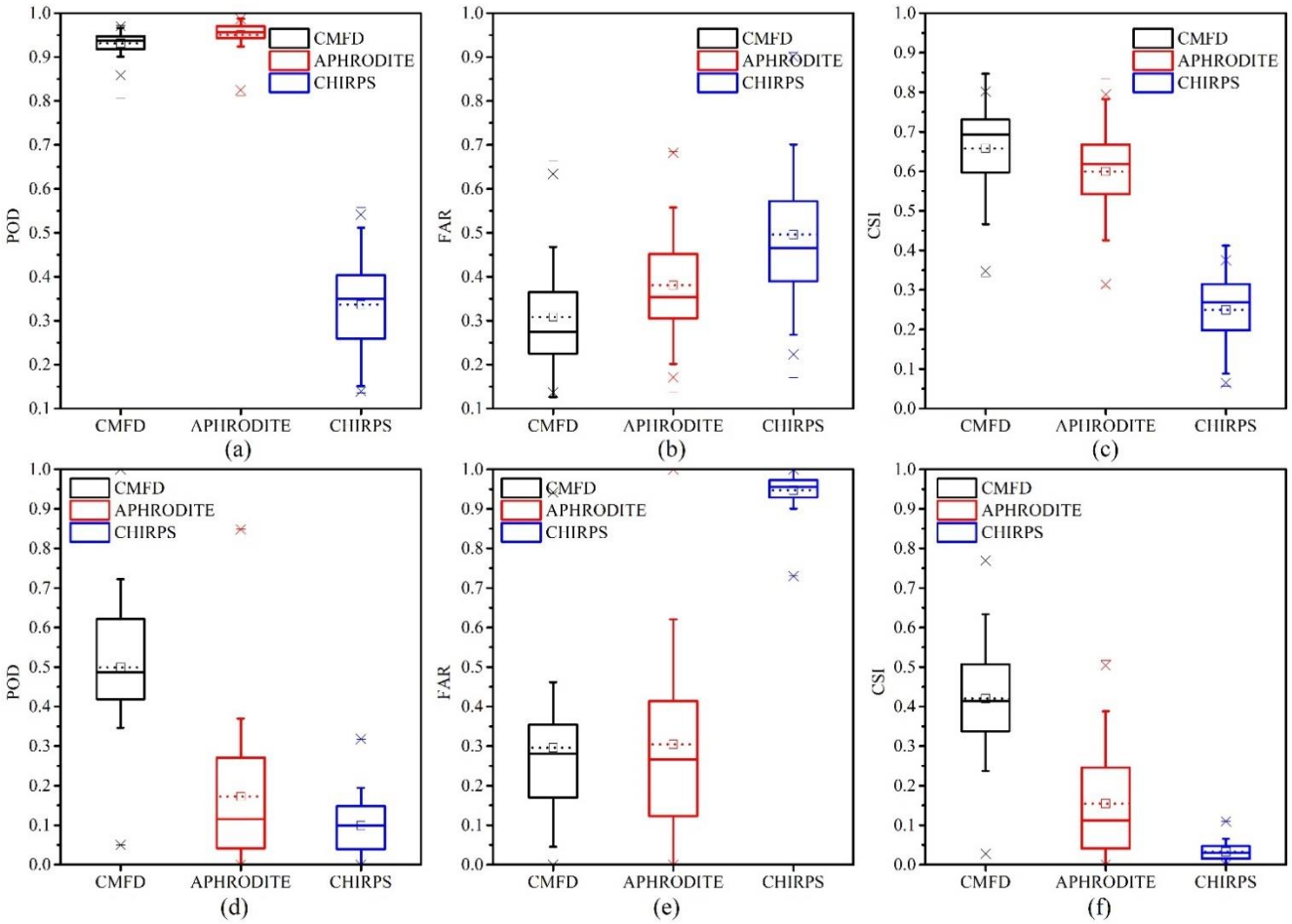

Figure 21. Boxplots of the POD, FAR, and CSI for general rain events (**a**–**c**) and heavy and extreme rain events (**d**–**f**) as derived from CMFD, APHRODITE, and CHIRPS at 101 rain gauges, respectively.

4. Discussion

In this study, a point-to-pixel validation method was conducted by comparing the gridded precipitation products and rain-gauge observations. Among the three products, CMFD generally outperformed the APHRODITE and CHIRPS datasets, which may be attributed to the GLDAS dataset and meteorological observations which were applied to generate the precipitation data [28]. Results also suggested that the CHIRPS dataset tended to overestimate precipitation compared to the rain-gauge stations in the QTP. Our findings are consistent with the results of previous studies by Liu, et al. [9], Wu, et al. [10], and Tan, et al. [11] for CHIRPS and APHRODITE in the QTP. It was reported that APHRODITE and CHIRPS in the QTP with POD values of 0.90 and 0.38, FAR values of 0.34 and 0.58, and CSI values of 0.63 and 0.28, respectively [11]. In this study, POD values were 0.95 and 0.34, FAR values were 0.38 and 0.50, and CSI values were 0.60 and 0.25 for APHRODITE and CHIRPS, respectively.

Several studies have also indicated that the application of gridded precipitation products on the QTP have some profound uncertainties and shortcomings compared to other regions. This could be partly because of the small number of rain-gauge stations on the QTP of which the data were merged to generate the gridded precipitation products [36,37]. In addition, climate conditions and topography may have a considerable influence on the spatial distribution of precipitation in QTP [36]. Previous studies have revealed that altitude affects precipitation; particularly, in complex mountainous terrain, the precipitation distribution is greatly affected by topographic elevation [38,39]. This may be one of the reasons for the poor performance of gridded precipitation products in the QTP.

Therefore, the downscaling technique focusing on topography can be employed to increase the accuracy of small-scale satellite precipitation.

5. Conclusions

This study aimed to examine the capability of three gridded precipitation products namely, CMFD, APHRODITE, and CHIRPS, for the detection of spatiotemporal patterning of extreme precipitation events over the QTP. We adopted a point-to-pixel approach and four accuracy indices, CC, RMSE, MAE and KGE, to evaluate the performance of the datasets by comparing to 101 rain-gauge stations throughout the region, and the major conclusions are summarized as follows:

Firstly, based on the results of fixed threshold indices, CDD, CWD, R10mm, and R20mm, CMFD could capture the spatial distribution of R10mm most accurately, while none of the three products were able to accurately depict CWD. Results of R10mm and R20mm suggested that all products depicted similar spatial patterns as OBS data, although CMFD maintained the highest CC and KGE scores and lowest RMSE and MAE values.

Secondly, analysis based on the station-related threshold indices, R95p, R99p, R95pTOT, and R99pTOT, revealed that CMFD and APHRODITE underestimated whereas CHIRPS overestimated these indices across the QTP. Results of R95p indicated that CMFD had the most accurate spatial error metrics; however, R99p, R95pTOT, and R99pTOT results indicated that none of the three gridded products could accurately capture these indices.

Thirdly, analysis based on the non-threshold indices, PRCPTOT, Rx1day, Rx5day, and SDII, revealed that all datasets showed a strong performance for PRCPTOT, CMFD and APHRODITE slightly underestimated the remaining three indices over the QTP, while CHIRPS values were severely overestimated.

Fourthly, the analysis of temporal patterning of extreme precipitation revealed that CMFD and APHRODITE tended to slightly underestimate most extreme precipitation indices, while CHIRPS strongly overestimated most indices. Our results further suggested that CMFD outperformed the other datasets at capturing most extreme precipitation indices over the QTP.

Finally, in rain occurrence, both CMFD and APHRODITE had the strong ability to detect general rain events correctly, with a high POD (0.93,0.95) and a low FAR (0.31,0.38), respectively, and CSI represented similar results with the POD. All of three gridded products had a weak ability in detecting heavy and extreme rain events.

This study demonstrated that CMFD had the greatest application potential for the climatological and risk analyses of extreme precipitation events over the QTP. Future development of high-resolution precipitation data will enhance the utility of the satellite-based products; CHIRPS is still the most ideal dataset for flood or drought monitoring. Future work should focus on developing an integrated hydrological research model that could accurately analyze regional climate comparisons for satellite and gauge-station derived observational data on an hourly basis.

Author Contributions: Conceptualization and methodology: J.Y. and Q.H.; data resources and curation: Q.H., H.C. and J.L.; analysis: J.Y., Q.H. and Q.J.; visualization: Q.H., Y.W. and F.T.; writing—original draft preparation: Q.H.; writing—review and editing: Q.H., J.Y. and J.L.; funding acquisition: J.Y. All authors have read and agreed to the published version of the manuscript.

Funding: This research was supported by the National Key Research and Development Program of China (Grant No.2016YFA0602404), the Strategic Priority Research Program of Chinese Academy of Sciences (Grant No. XDA23060704).

Institutional Review Board Statement: Not applicable.

Informed Consent Statement: Not applicable.

Data Availability Statement: The data presented in this study are available on request from the corresponding author.

Acknowledgments: The authors would like to thank all the providers of the precipitation products for free; we would also like to thank the reviewers and editors who provided valuable comments and suggestions for this paper.

Conflicts of Interest: The authors have no conflicts of interest to declare.

Appendix A

See Tables A1–A3.

Table A1. Geographical locations and elevations of gauging stations used in the present study.

NO.	Station-ID	Long (°N)	Lat (°E)	Altitude (m)	NO.	Station-ID	Long (°N)	Lat (°E)	Altitude (m)
1	51,804	75.23	37.77	3090.10	52	56,021	95.78	34.13	4175.00
2	51,886	90.85	38.25	2944.80	53	56,029	97.02	33.02	3681.20
3	52,633	98.42	38.80	3367.00	54	56,033	98.22	34.92	4272.30
4	52,645	99.58	38.42	3320.00	55	56,034	97.13	33.80	4415.40
5	52,657	100.25	38.18	2787.40	56	56,038	98.10	32.98	4200.00
6	52,707	93.68	36.80	2767.00	57	56,043	100.25	34.47	3719.00
7	52,713	95.37	37.85	3173.20	58	56,046	99.65	33.75	3967.50
8	52,737	97.37	37.37	2981.50	59	56,065	101.60	34.73	3500.00
9	52,754	100.13	37.33	3301.50	60	56,067	101.48	33.43	3628.50
10	52,765	101.62	37.38	2850.00	61	56,074	102.08	34.00	3471.40
11	52,787	102.87	37.20	3045.10	62	56,079	102.97	33.58	3439.60
12	52,818	94.90	36.42	2807.60	63	56,080	102.90	35.00	2910.00
13	52,825	96.42	36.43	2790.40	64	56,106	93.78	31.88	4022.80
14	52,833	98.48	36.92	2950.00	65	56,109	93.78	31.48	3940.00
15	52,836	98.10	36.30	3191.10	66	56,116	95.60	31.42	3873.10
16	52,842	99.08	36.78	3087.60	67	56,125	96.48	32.20	3643.70
17	52,856	100.62	36.27	2835.00	68	56,128	96.60	31.22	3810.00
18	52,866	101.75	36.72	2295.20	69	56,137	97.17	31.15	3306.00
19	52,868	101.43	36.03	2237.10	70	56,144	98.58	31.80	3184.00
20	52,876	102.85	36.32	1813.90	71	56,146	100.00	31.62	3393.50
21	52,908	93.08	35.22	4612.20	72	56,151	100.75	32.93	3530.00
22	52,943	99.98	35.58	3323.20	73	56,152	100.33	32.28	3893.90
23	52,955	100.75	35.58	3120.00	74	56,167	101.12	30.98	2957.20
24	52,957	100.60	35.25	3148.20	75	56,172	102.23	31.90	2664.40
25	52,968	101.47	35.03	3662.80	76	56,173	102.55	32.80	3491.60
26	52,974	102.02	35.52	2491.40	77	56,178	102.35	31.00	2369.20
27	55,228	80.08	32.50	4278.60	78	56,182	103.57	32.65	2850.70
28	55,248	84.42	32.15	4414.90	79	56,202	93.28	30.67	4488.80
29	55,279	90.02	31.38	4700.00	80	56,223	95.83	30.75	3640.00
30	55,294	91.10	32.35	4800.00	81	56,227	95.77	29.87	2736.00
31	55,299	92.07	31.48	4507.00	82	56,228	96.92	30.05	3260.00
32	55,437	81.25	30.28	4900.00	83	56,247	99.10	30.00	2589.20
33	55,472	88.63	30.95	4672.00	84	56,251	100.32	30.93	3000.00
34	55,493	91.10	30.48	4200.00	85	56,257	100.27	30.00	3948.90
35	55,569	87.60	29.08	4000.00	86	56,307	92.58	29.15	3260.00
36	55,572	89.10	29.68	4000.00	87	56,312	94.33	29.67	2991.80
37	55,578	88.88	29.25	3836.00	88	56,317	94.22	29.22	2950.00
38	55,585	90.17	29.43	3809.40	89	56,331	97.83	29.67	3780.00
39	55,589	90.98	29.30	3555.30	90	56,342	98.60	29.68	3870.00
40	55,591	91.13	29.67	3648.90	91	56,357	100.30	29.05	3727.70
41	55,593	91.73	29.85	3804.30	92	56,374	101.97	30.05	2615.70
42	55,598	91.77	29.25	3551.70	93	56,434	97.47	28.65	2327.60
43	55,655	85.97	28.18	3810.00	94	56,444	98.92	28.48	3319.00
44	55,664	87.08	28.63	4300.00	95	56,459	101.27	27.93	2426.50
45	55,680	89.60	28.92	4040.00	96	56,462	101.50	29.00	2987.30
46	55,681	90.40	28.97	4431.70	97	56,533	98.67	27.75	1583.30
47	55,690	91.95	27.98	4280.30	98	56,543	99.70	27.83	3276.70
48	55,696	92.47	28.42	3860.00	99	56,548	99.28	27.17	2326.10
49	55,773	89.08	27.73	4300.00	100	56,565	101.52	27.43	2545.00
50	56,004	92.43	34.22	4533.10	101	56,651	100.22	26.87	2392.40
51	56,018	95.30	32.90	4066.40					

Table A2. Statistical metrics of annual extreme precipitation estimates derived from CMFD, APHRODITE, and CHIRPS for the period 1981–2014 with reference to gauge observations.

Indices	Datasets	CC	MAE	RMSE	KGE
CDD	CMFD	0.85	16.69	27.55	0.82
	APHRODITE	0.78	20.68	31.86	0.77
	CHIRPS	0.37	54.12	56.56	0.30
CWD	CMFD	0.67	2.87	4.04	0.53
	APHRODITE	0.64	6.07	5.67	0.21
	CHIRPS	0.38	3.17	3.52	0.31
R10mm	CMFD	0.94	2.69	3.07	0.81
	APHRODITE	0.85	5.79	3.99	0.49
	CHIRPS	0.72	5.99	7.26	0.54
R20mm	CMFD	0.90	1.19	1.44	0.59
	APHRODITE	0.75	2.32	1.25	0.36
	CHIRPS	0.57	3.55	4.42	0.22
R95p	CMFD	0.88	25.87	37.19	0.87
	APHRODITE	0.77	35.05	40.63	0.72
	CHIRPS	0.46	59.86	73.47	0.46
R95pT0T	CMFD	0.73	5.46	7.30	0.72
	APHRODITE	0.58	6.94	9.04	0.56
	CHIRPS	0.13	11.56	14.44	0.13
R99p	CMFD	0.73	16.72	26.06	0.73
	APHRODITE	0.63	18.83	27.75	0.58
	CHIRPS	0.19	35.54	49.64	0.20
R99pTOT	CMFD	0.64	3.39	5.63	0.53
	APHRODITE	0.58	3.79	5.90	0.21
	CHIRPS	0.08	6.95	10.14	0.31
PRCPTOT	CMFD	0.98	25.41	50.20	0.97
	APHRODITE	0.95	60.28	68.53	0.87
	CHIRPS	0.78	108.33	167.17	0.75
Rx1day	CMFD	0.88	5.08	6.37	0.53
	APHRODITE	0.77	10.38	5.60	0.21
	CHIRPS	0.51	17.71	18.34	0.31
Rx5day	CMFD	0.95	6.14	8.99	0.92
	APHRODITE	0.87	14.43	9.77	0.72
	CHIRPS	0.61	21.19	27.40	0.56
SDII	CMFD	0.89	0.85	0.62	0.82
	APHRODITE	0.80	1.62	0.62	0.67
	CHIRPS	0.58	3.80	4.11	0.46

Table A3. Mean categorical verification statistics: POD, FAR and CSI for detecting different rain events derived from CMFD, APHRODITE, and CHIRPS for the period 1981–2014.

	Datasets	POD	FAR	CSI
General rain events (with daily precipitation amount < 20 mm)	CMFD	0.931	0.308	0.657
	APHRODITE	0.950	0.381	0.599
	CHIRPS	0.336	0.496	0.250
Heavy and extreme rain events (with daily precipitation amount $\geq$ 20mm)	CMFD	0.489	0.293	0.416
	APHRODITE	0.173	0.289	0.152
	CHIRPS	0.097	0.919	0.032

References

1. Cao, L.; Pan, S. Changes in precipitation extremes over the "Three-River Headwaters" region, hinterland of the Tibetan Plateau, during 1960–2012. *Quat. Int.* **2014**, *321*, 105–115. [CrossRef]
2. Katsanos, D.; Retalis, A.; Tymvios, F.; Michaelides, S. Analysis of precipitation extremes based on satellite (CHIRPS) and in situ dataset over Cyprus. *Nat. Hazards* **2016**, *83*, 53–63. [CrossRef]
3. Cui, P.; Dang, C.; Cheng, Z.; Scott, K.M. Debris flows resulting from glacial-lake outburst floods in Tibet, China. *Phys. Geogr.* **2010**, *31*, 508–527. [CrossRef]
4. Wang, S.; Che, Y.; Xinggang, M. Integrated risk assessment of glacier lake outburst flood (GLOF) disaster over the Qinghai–Tibetan Plateau (QTP). *Landslides* **2020**, *17*, 2849–2863. [CrossRef]
5. Xu, Z.; Wu, Z.; He, H.; Wu, X.; Zhou, J.; Zhang, Y.; Guo, X. Evaluating the accuracy of MSWEP V2.1 and its performance for drought monitoring over mainland China. *Atmos. Res.* **2019**, *226*, 17–31. [CrossRef]
6. Alexander, L.V.; Bador, M.; Roca, R.; Contractor, S.; Donat, M.G. Intercomparison of annual precipitation indices and extremes over global land areas from in situ, space-based and reanalysis products. *Environ. Res. Lett.* **2020**, *15*, 055002. [CrossRef]
7. Ward, P.J.; Blauhut, V.; Bloemendaal, N.; Daniell, J.E.; de Ruiter, M.C.; Duncan, M.J.; Emberson, R.; Jenkins, S.; Kirschbaum, D.; Kunz, M.; et al. Review article: Natural hazard risk assessments at the global scale. *Nat. Hazards Earth Syst. Sci.* **2020**, *20*, 1069–1096. [CrossRef]
8. Bai, L.; Shi, C.; Li, L.; Yang, Y.; Wu, J. Accuracy of CHIRPS Satellite-Rainfall Products over Mainland China. *Remote. Sens.* **2018**, *10*, 362. [CrossRef]
9. Liu, J.; Shangguan, D.; Liu, S.; Ding, Y.; Wang, S.; Wang, X. Evaluation and comparison of CHIRPS and MSWEP dai-ly-precipitation products in the Qinghai-Tibet Plateau during the period of 1981–2015. *Atmos. Res.* **2019**, *230*, 104634. [CrossRef]
10. Wu, Y.; Guo, L.; Zheng, H.; Zhang, B.; Li, M. Hydroclimate assessment of gridded precipitation products for the Tibetan Plateau. *Sci. Total. Environ.* **2019**, *660*, 1555–1564. [CrossRef]
11. Tan, X.; Ma, Z.; He, K.; Han, X.; Ji, Q.; He, Y. Evaluations on gridded precipitation products spanning more than half a century over the Tibetan Plateau and its surroundings. *J. Hydrol.* **2020**, *582*, 124455. [CrossRef]
12. Zhang, S.; Wang, D.; Qin, Z.; Zheng, Y.; Guo, J. Assessment of the GPM and TRMM Precipitation Products Using the Rain Gauge Network over the Tibetan Plateau. *J. Meteorol. Res.* **2018**, *32*, 324–336. [CrossRef]
13. Wang, X.; Ding, Y.; Zhao, C.; Wang, J. Similarities and improvements of GPM IMERG upon TRMM 3B42 precipitation product under complex topographic and climatic conditions over Hexi region, Northeastern Tibetan Plateau. *Atmos. Res.* **2019**, *218*, 347–363. [CrossRef]
14. Guo, J.; Zhai, P.; Wu, L.; Cribb, M.; Li, Z.; Ma, Z.; Wang, F.; Chu, D.; Wang, P.; Zhang, J. Diurnal variation and the influential factors of precipitation from surface and satellite measurements in Tibet. *Int. J. Clim.* **2013**, *34*, 2940–2956. [CrossRef]
15. Mei, Y.; Nikolopoulos, E.I.; Anagnostou, E.N.; Borga, M. Evaluating satellite precipitation error propagation in runoff simulations of mountainous basins. *J. Hydrometeorol.* **2016**, *17*, 1407–1423. [CrossRef]
16. Derin, Y.; Yilmaz, K.K. Evaluation of Multiple Satellite-Based Precipitation Products over Complex Topography. *J. Hydrometeorol.* **2014**, *15*, 1498–1516. [CrossRef]
17. Bhuiyan, M.; Nikolopoulos, E.I.; Anagnostou, E.N. Machine learning-based blending of satellite and reanalysis precipitation datasets: A multiregional tropical complex terrain evaluation. *J. Hydrometeorol.* **2019**, *20*, 2147–2161. [CrossRef]
18. Huang, X.; Wang, D.; Liu, Y.; Feng, Z.; Wang, D. Evaluation of extreme precipitation based on satellite retrievals over China. *Front. Earth Sci.* **2017**, *12*, 846–861. [CrossRef]
19. Timmermans, B.; Wehner, M.; Cooley, D.; O'Brien, T.; Krishnan, H. An evaluation of the consistency of extremes in gridded precipitation data sets. *Clim. Dyn.* **2019**, *52*, 6651–6670. [CrossRef]
20. Cavalcante, R.B.L.; Ferreira, D.B.D.S.; Pontes, P.R.; Tedeschi, R.G.; da Costa, C.P.W.; de Souza, E. Evaluation of extreme rainfall indices from CHIRPS precipitation estimates over the Brazilian Amazonia. *Atmos. Res.* **2020**, *238*, 104879. [CrossRef]
21. Harrison, L.; Funk, C.; Peterson, P. Identifying changing precipitation extremes in Sub-Saharan Africa with gauge and satellite products. *Environ. Res. Lett.* **2019**, *14*, 085007. [CrossRef]
22. Supari; Tangang, F.; Juneng, L.; Cruz, F.; Chung, J.X.; Ngai, S.T.; Salimun, E.; Mohd, M.S.F.; Santisirisomboon, J.; Singhruck, P. Multi-model projections of precipitation extremes in Southeast Asia based on CORDEX-Southeast Asia simulations. *Environ. Res.* **2020**, *184*, 109350. [CrossRef]
23. Zhou, B.; Xu, Y.; Wu, J.; Dong, S.; Shi, Y. Changes in temperature and precipitation extreme indices over China: Analysis of a high-resolution grid dataset. *Int. J. Clim.* **2015**, *36*, 1051–1066. [CrossRef]
24. Miao, C.; Ashouri, H.; Hsu, K.-L.; Sorooshian, S.; Duan, Q. Evaluation of the PERSIANN-CDR Daily Rainfall Estimates in Capturing the Behavior of Extreme Precipitation Events over China. *J. Hydrometeorol.* **2015**, *16*, 1387–1396. [CrossRef]
25. Zhao, G.; Zhai, J.; Tian, P.; Zhang, L.; Mu, X.; An, Z.; Han, M. Variations in extreme precipitation on the Loess Plateau using a high-resolution dataset and their linkages with atmospheric circulation indices. *Theor. Appl. Clim.* **2017**, *133*, 1235–1247. [CrossRef]
26. Xi, Y.; Miao, C.; Wu, J.; Duan, Q.; Lei, X.; Li, H. Spatiotemporal Changes in Extreme Temperature and Precipitation Events in the Three-Rivers Headwater Region, China. *J. Geophys. Res. Atmos.* **2018**, *123*, 5827–5844. [CrossRef]
27. Ren, Z.; Zhao, P.; Zhang, Q.; Zhang, Z.; Cao, L.; Yang, Y. Quality control procedures for hourly precipitation data from automatic weather stations in China (in Chinese). *Meteorol. Mon.* **2010**, *36*, 123–132.

28. He, J.; Yang, K.; Tang, W.; Lu, H.; Qin, J.; Chen, Y.; Li, X. The first high-resolution meteorological forcing dataset for land process studies over China. *Sci. Data* **2020**, *7*, 1–11. [CrossRef]
29. Liu, Y.; Xu, J.; Lu, X.; Nie, L. Assessment of glacier- and snowmelt-driven streamflow in the arid middle Tianshan Mountains of China. *Hydrol. Process.* **2020**, *34*, 2750–2762. [CrossRef]
30. Yatagai, A.; Kamiguchi, K.; Arakawa, O.; Hamada, A.; Yasutomi, N.; Kitoh, A. APHRODITE: Constructing a Long-Term Daily Gridded Precipitation Dataset for Asia Based on a Dense Network of Rain Gauges. *Bull. Am. Meteorol. Soc.* **2012**, *93*, 1401–1415. [CrossRef]
31. Funk, C.; Peterson, P.; Landsfeld, M.; Pedreros, D.; Verdin, J.; Shukla, S.; Husak, G.; Rowland, J.; Harrison, L.; Hoell, A.; et al. The climate hazards infrared precipitation with stations—A new environmental record for monitoring extremes. *Sci. Data* **2015**, *2*, 1–21. [CrossRef] [PubMed]
32. Zhang, X.; Alexander, L.; Hegerl, G.; Jones, P.; Tank, A.K.; Peterson, T.C.; Trewin, B.; Zwiers, F.W. Indices for monitoring changes in extremes based on daily temperature and precipitation data. *Wiley Interdiscip. Rev. Clim. Chang.* **2011**, *2*, 851–870. [CrossRef]
33. Karl, T.R.; Nicholls, N.; Ghazi, A. CLIVAR/GCOS/WMO Workshop on Indices and Indicators for Climate Extremes Workshop Summary BT-Weather and Climate Extremes: Changes, Variations and a Perspective from the Insurance Industry. In *Weather and Climate Extremes*; Springer: Dordrecht, The Netherlands, 1999; pp. 3–7.
34. Peterson, T.C.; Manton, M.J. Monitoring Changes in Climate Extremes: A Tale of International Collaboration. *Bull. Am. Meteorol. Soc.* **2008**, *89*, 1266–1271. [CrossRef]
35. Wang, H.; Shao, Z.; Gao, T.; Zou, T.; Liu, J.; Yuan, H. Extreme precipitation event over the Yellow Sea western coast: Is there a trend? *Quat. Int.* **2017**, *441*, 1–17. [CrossRef]
36. Yong, B.; Liu, D.; Gourley, J.J.; Tian, Y.; Huffman, G.J.; Ren, L.; Hong, Y. Global View of Real-Time Trmm Multisatellite Precipitation Analysis: Implications for Its Successor Global Precipitation Measurement Mission. *Bull. Am. Meteorol. Soc.* **2015**, *96*, 283–296. [CrossRef]
37. Beck, H.E.; Vergopolan, N.; Pan, M.; Levizzani, V.; van Dijk, A.I.J.M.; Weedon, G.P.; Brocca, L.; Pappenberger, F.; Huffman, G.J.; Wood, E.F. Global-scale evaluation of 22 precipitation datasets using gauge observations and hydrological modeling. *Hydrol. Earth Syst. Sci.* **2017**, *21*, 6201–6217. [CrossRef]
38. Kumari, M.; Singh, C.K.; Bakimchandra, O.; Basistha, A. Geographically weighted regression based quantification of rainfall-topography relationship and rainfall gradient in Central Himalayas. *Int. J. Climatol.* **2017**, *37*, 1299–1309. [CrossRef]
39. Hughes, M.; Hall, A.; Fovell, R.G. Blocking in areas of complex topography, and its influence on rainfall distribution. *J. Atmos. Sci.* **2013**, *66*, 508–518. [CrossRef]